J. Fluid Mech. (2022), *vol*. 937, A25, doi:10.1017/jfm.2022.57

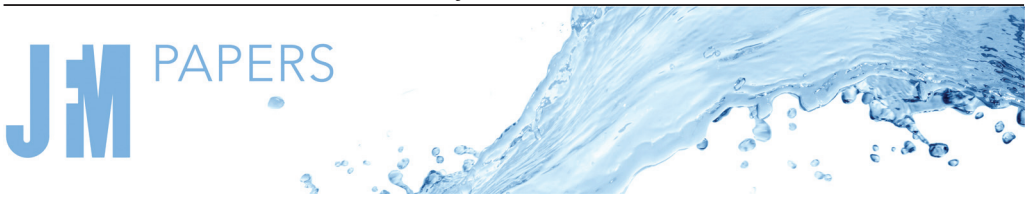

Analysis of turbulent coagulation in a jet with discretised population balance and DNS

Malamas Tsagkaridis[1], **Stelios Rigopoulos**[1,†] **and George Papadakis** [2]

[1]Department of Mechanical Engineering, Imperial College London, Exhibition Road, London SW7 2AZ, UK

[2]Department of Aeronautics, Imperial College London, Exhibition Road, London SW7 2AZ, UK

(Received 8 May 2021; revised 17 December 2021; accepted 16 January 2022)

The objective of the present study is to investigate turbulence–coagulation interaction via direct numerical simulation (DNS) coupled with the population balance equation (PBE). Coagulation is an important process in several environmental and engineering applications involving turbulent flow, including soot formation, gas-phase synthesis of nanoparticles and atmospheric processes, but its interaction with turbulence is not yet fully understood. Particle dynamics can be described by the PBE, whose Reynolds decomposition leads to unclosed terms involving correlations of number density fluctuations. In this work, we employ a discretisation (sectional) method for the solution of the PBE, which is free of *a priori* assumptions regarding the particle size distribution (PSD), and couple it with a DNS for the flow field in order to study the behaviour and significance of the unknown correlations. At present, it is not feasible to resolve the Batchelor scales that result from diffusion at high Schmidt number, hence a unity Schmidt number is employed. The investigation is conducted on a three-dimensional planar jet laden with monodisperse nanoparticles, and coagulation in the free-molecule regime is considered. The correlations due to turbulent fluctuations of the particle number density are calculated at several points in the domain and found to be positive in most cases, except close to the jet break-up. The transport equation for the moments of the PSD is also studied, and it is found that the correlations make a considerable contribution to the time-averaged coagulation source term, up to 20 % on the jet centreline and 40 % close to the edges.

Key words: turbulent reacting flows, aerosols/atomization, breakup/coalescence

1. Introduction

Aerosols constitute dispersions of fine particles or droplets in gases, and are encountered in many natural and engineering processes. Examples include soot or carbon black formation

† Email address for correspondence: s.rigopoulos@imperial.ac.uk

(Rigopoulos 2010, 2019; Raman & Fox 2016), flame synthesis of nanoparticles (Buesser & Pratsinis 2012; Goudeli & Pratsinis 2016), sulphur-driven particle formation in exhaust systems (Olin, Rönkkö & Dal Maso 2015), and atmospheric processes (Kulmala *et al.* 2004). Aerosols are polydisperse due to phenomena such as coagulation, condensation and evaporation, and their polydispersity is characterised by the particle size distribution (PSD). Aerosol dynamics can be described by the population balance equation (PBE), also known as the general dynamic equation (GDE), which is an equation that describes the spatial and temporal evolution of the PSD due to convective transport as well as physical and chemical processes such as coagulation and condensation.

Coagulation occurs in several contexts such as atmospheric aerosols, cloud formation, flame synthesis of nanoparticles and combustion aerosols originating from sources such as incinerators and pulverised combustion units (Friedlander 2000). In particular, coagulation is the dominant mechanism in aerosol synthesis of nanomaterials such as fumed silica (SiO_2), pigmentary titania (TiO_2) and zinc oxide (ZnO) vulcanising catalysts (Buesser & Pratsinis 2012). In most cases, particle formation and coagulation occur in turbulent flows. The complexity of turbulence and the nonlinear interactions involved in the aerosol processes render the resulting problem intractable via simplified methods. The objective of this study is to employ direct numerical simulation (DNS) of turbulence coupled with a discretised form of the PBE as a numerical tool for studying the turbulence–coagulation interaction.

The effect of turbulence on coagulation is manifested in two ways. The first is associated with the collision mechanism, which is substantially different in turbulent flows depending on the particle size and inertia. This problem was first studied by Saffman & Turner (1956) and Levich (1962), who proposed expressions for the turbulent coagulation kernel. Numerous works, including Delichatsios & Probstein (1975), Wang, Wexler & Zhou (1998) and Reade & Collins (2000), investigated experimentally and numerically the collision mechanism in turbulent flows and the assumptions inherent in the expressions for the kernels proposed.

The present study is concerned with the second, and rather less studied, effect of turbulence on coagulation, which is the influence of fluctuations in the particle number density. This is the 'closure problem' of turbulence for aerosols, and it arises from the nonlinear interactions between number densities of particles of different sizes that appear within the PBE for coagulation. Early discussions of this problem appear in the works of Levin & Sedunov (1966,1968), Scott (1967) and Warshaw (1967). These studies were concerned with turbulent coagulation in the context of coalescing cloud droplets and were reviewed by Drake (1972). More specifically, Levin & Sedunov (1968) dropped the correlations due to the coagulation source term because of the lack of knowledge at that time regarding the fluctuations in the collision integral, while Warshaw (1967) assumed that the correlations can be neglected in the case of a very large cloud volume. Friedlander (2000) also stated that the importance of these terms has not been carefully studied, while Drossinos & Housiadas (2006) mentioned that more attention must be given to the PBE in turbulent flows.

The first study of coagulation with a DNS–PBE approach was done by Settumba & Garrick (2003), where simulations of a two-dimensional (2-D) incompressible temporal mixing layer were performed. A moment method, which requires *a priori* assumptions on the shape of the PSD, was used to describe the coagulating aerosol. A coagulation Damköhler number was also defined, which represents the ratio of the convection to coagulation time scales.

A nodal method that makes no *a priori* assumptions regarding the PSD was used by Miller & Garrick (2004) for their simulations of nanoparticle coagulation in a 2-D

turbulent planar jet. They showed that large-scale vortical structures perturb the PSD from the self-preserving distribution and lead to particle distributions with larger geometric standard deviations. However, the computation of turbulent fluctuations that occur when decomposing the particle concentration field into time-averaged and fluctuations (in the context of Reynolds-averaged Navier-Stokes (RANS)) or resolved and subgrid components (in the context of large-eddy simulation (LES)) was left for future work. Garrick, Lehtinen & Zachariah (2006) performed further DNS of nanoparticle coagulation in a 2-D temporal mixing layer, where a nodal representation with 12 bins was used. An increase in the coagulation Damköhler number was found to result in an increase in particle growth and in prediction of PSDs wider than the self-preserving limit. It was concluded that three-dimensional (3-D) simulations, where vortex tilting and stretching can occur, are needed to fully understand the effects of turbulence on the PSD.

The interaction of turbulence with nanoparticle coagulation was studied by Garrick (2011). Coagulation was the sole aerosol mechanism in a 3-D turbulent shear flow. A method of moments, which assumes that the PSD is log-normal, was employed to describe the particle field. The particle growth rate was decomposed into large- and small-scale interactions in order to investigate the effect of the flow dynamics and the coagulation Damköhler number. The DNS results showed that small-scale interactions act to both increase and decrease particle growth. Furthermore, probability density functions (PDFs) conditioned on the Q-criterion suggested that in rotation-dominated regions, the effect of the small-scale interactions is primarily to reduce particle growth.

The effect of turbulence on nanoparticle growth in turbulent reacting flows was studied by Das & Garrick (2010). A nodal approach with 22 ‘bins’ was utilised to describe nucleation, condensation and coagulation in a planar turbulent jet via DNS. Instantaneous, filtered and spanwise averaged data of the particle field were computed in order to examine the nature of the unresolved contributions (turbulent fluctuations) on particle growth. The effect of turbulence on particle dynamics was assessed by decomposing the particle growth rate in averaged and fluctuating components (in the context of RANS) and filtered and unresolved components (in the context of LES). The results revealed that the unresolved small-scale fluctuations can both augment and inhibit particle growth, but the predominant effect is to reduce particle growth. That research concluded that turbulence or subgrid scale (SGS) models are needed for accurately simulating particle dynamics in turbulent flows.

One of the few experimental studies of nanoparticle coagulation in turbulent flows was done by Junzong, Haiying & Jinsheng (2013). The authors studied silica SiO_2 nanoparticle dispersion and coagulation in a high-Reynolds-number round jet. It was shown that there is an intermediate region across the centreline with high turbulence intensity where the Sauter mean diameter, which was used to characterise particle size, increases, and this was attributed to the turbulence coagulation effect, where turbulent vortices promote coagulation. The experimental configuration of Junzong *et al.* (2013) was investigated numerically by Pesmazoglou, Kempf & Navarro-Martinez (2017), where a stochastic aggregation model based on a Lagrangian framework was applied in the context of LES. The results showed good agreement with the experiments. However, the authors concluded that for this configuration, aggregation did not play a big role since no significant differences were found by including or excluding the aggregation model.

One of the first attempts to model the effect of turbulent fluctuations on the PBE was made by Rigopoulos (2007), where a probability density function (PDF) approach, which overcomes the closure problem, was developed and tested in a partially stirred reactor. It was concluded that future work should evaluate the error that occurs by neglecting the turbulent fluctuations of the PSD in particle formation/coagulation problems. Later work

studied these fluctuations in nucleation-growth problems via the PBE–PDF method in RANS (Di Veroli & Rigopoulos 2009, 2010, 2011; Rigopoulos 2010) and LES (Sewerin & Rigopoulos 2017, 2018, 2019). The PBE in turbulent flow was also studied via coupling with DNS in the context of a nucleation-growth problem by Tang, Rigopoulos & Papadakis (2020). However, none of these studies included coagulation.

From the preceding review, it can be concluded that the turbulence–coagulation interaction is not yet fully understood. This paper aims to study in more detail this interaction, and in particular to shed light on the long-standing problem of the unknown correlations that arise in the Reynolds decomposition of the PBE. The behaviour and significance of these correlations are investigated by performing DNS of a 3-D spatially developing planar jet laden with monodisperse nanoparticles. This flow case is relevant to many engineering and environmental processes involving particle coagulation (gas-phase synthesis of nanoparticles, plumes with particulate emissions). The mathematical methodology used for the characterisation of the nanoparticle dynamics is the PBE coupled with DNS, and thus results in a fully Eulerian description of aerosol dynamics in a turbulent flow. The PBE is solved via a recently proposed discretisation method (Liu & Rigopoulos 2019), and the whole distribution is retrieved without any assumptions about its shape. By keeping the approach model-free, we aim to focus on the turbulence–coagulation interaction and draw conclusions that will aid the development of new models. The findings of the study are relevant to any problem featuring turbulence and coagulation, such as soot formation and nanoparticle synthesis. However, in such problems, it is difficult to distinguish the result of this interaction from other effects, particularly those associated with chemical kinetic processes such as nucleation and growth. As a result, it is difficult to determine the contribution of this effect to discrepancies in comparisons between experimental and numerical results, which are usually attributed to different reasons. The present study is effectively a DNS-based computational experiment that isolates the effect of turbulence–coagulation interaction.

The rest of this paper is structured as follows. Section 2 presents the governing equations, the numerical solution method, and details on the flow configuration and the computational setup. Subsequently, in § 3, results for the flow field are validated with experimental and other reference DNS data, while results of the particle field are validated by comparing the PSD with the theoretical self-preserving distribution. The results are presented and discussed in § 4, in the following order. First, the evolution of the moments and the effects of coagulation and turbulent mixing are discussed. Following this, the discussion focuses on the analysis of turbulent fluctuations of the number densities. Particular emphasis is given to the effect of the unknown correlations that occur when applying Reynolds decomposition to the transport equations of the zeroth and second moments. Finally, the conclusions are presented in § 5.

2. Methodology

2.1. *Governing equations*

The flow is assumed to be incompressible and isothermal, governed by the Navier–Stokes equations

$$\frac{\partial u_i^*}{\partial t^*} + u_j^* \frac{\partial u_i^*}{\partial x_j^*} = -\frac{\partial p^*}{\partial x_i^*} + \frac{1}{Re} \frac{\partial^2 u_i^*}{\partial x_j^* \, \partial x_j^*}, \tag{2.1}$$

$$\frac{\partial u_j^*}{\partial x_j^*} = 0, \tag{2.2}$$

where u_i^* is the Cartesian velocity component in the ith direction, and p^* is the pressure. The asterisk denotes non-dimensional variables, defined as

$$u_i^* = \frac{u_i}{U_o}, \quad p^* = \frac{p}{\rho U_o^2}, \quad x_i^* = \frac{x_i}{h}, \quad t^* = \frac{t}{h/U_o}, \tag{2.3a–d}$$

where U_o is the jet velocity, h is the jet width at the inlet, and ρ is the fluid density. The Reynolds number is defined as $Re = U_o h/\nu$, where ν is the kinematic viscosity.

The nanoparticle dynamics is described by the PBE, which assumes the form (Friedlander 2000)

$$\frac{\partial n}{\partial t} + u_j \frac{\partial n}{\partial x_j} = \frac{\partial}{\partial x_j}\left(D_p \frac{\partial n}{\partial x_j}\right) + \frac{1}{2}\int_0^v \beta(w, v-w)\, n(w)\, n(v-w)\, \mathrm{d}w - \int_0^\infty \beta(v, w)\, n(v)\, n(w)\, \mathrm{d}w, \tag{2.4}$$

where v and w denote particle volume, $n = n(\boldsymbol{x}, t, v)$ is the number density function per unit volume of fluid (such that $n\,\mathrm{d}v$ is the concentration of particles with volume between v and $v + \mathrm{d}v$), D_p is the diffusion coefficient of particles of volume v yielded by the Stokes–Einstein equation (Friedlander 2000), and $\beta(v, w)$ is the coagulation kernel, a function that represents the frequency of collisions that lead to coagulation events and will be discussed further below. Coagulation is described by the two integral terms in (2.4), which denote particle birth and death. The birth term accounts for all possible particle pairs whose coalescence results in particles of volume v, while the death term accounts for the disappearance of particles of volume v due to coagulation with particles of any volume. The PBE can include additional mechanisms representing nucleation, growth and breakage, but the focus of the present study is on coagulation.

When the particle diameter is much smaller than the mean free path of the carrier gas, the particles can be assumed to behave like rigid elastic spheres, and an expression for the collision frequency $\beta(v, w)$ can be derived from the kinetic theory of gases. In this case, coagulation takes place in the free-molecule regime and the kernel is

$$\beta(v, w) = A_1 \left(\frac{1}{v} + \frac{1}{w}\right)^{1/2} \left(v^{1/3} + w^{1/3}\right)^2, \tag{2.5}$$

with the factor A_1 defined as

$$A_1 = \left(\frac{3}{4\pi}\right)^{1/6} \left(\frac{6k_bT}{\rho_p}\right)^{1/2}, \tag{2.6}$$

where ρ_p is the particle density, T is the temperature, and k_b is the Boltzmann constant.

For future reference, we also present the transport equation for the moments of the distribution $n = n(\boldsymbol{x}, t, v)$. The kth moment, M_k, is defined as

$$M_k = \int_0^\infty v^k\, n(v)\, \mathrm{d}v. \tag{2.7}$$

Some of the low-order moments have a physical interpretation. For example, the zeroth moment, M_0, is the total number concentration of particles, while the first moment, M_1,

represents the particle volume fraction. Furthermore, when the diameter of the particles is smaller than the wavelength of the incident light, the second moment, M_2, is proportional to the total light scattering by particles (Friedlander 2000). The following transport equation for the evolution of M_k can be derived (Williams & Loyalka 1991; Whitby & McMurry 1997):

$$\frac{\partial M_k}{\partial t} + u_j \frac{\partial M_k}{\partial x_j} = \frac{\partial}{\partial x_j}\left(D_p \frac{\partial M_k}{\partial x_j}\right) + \frac{1}{2}\int_0^\infty \int_0^\infty (v+w)^k \, \beta(v,w)\, n(v)\, n(w)\, \mathrm{d}v\, \mathrm{d}w - \frac{1}{2}\int_0^\infty \int_0^\infty (v^k + w^k)\, \beta(v,w)\, n(v)\, n(w)\, \mathrm{d}v\, \mathrm{d}w. \tag{2.8}$$

In the absence of convection and diffusion (i.e. in a perfectly stirred reactor), it can be shown that (2.4) admits self-similar solutions. It must be noted that M_1 is constant under these conditions. If the number density function and particle volume are scaled as

$$\psi = \frac{M_1}{M_0^2}\, n, \tag{2.9}$$

$$\eta = \frac{M_0}{M_1}\, v, \tag{2.10}$$

and substituted in (2.4), then the solution reaches a time-independent distribution $\psi(\eta)$ after a sufficient amount of time. The initial particle distribution affects the time to reach the self-preserving (SP) state but not the distribution itself (Friedlander 2000). For an initially monodisperse aerosol undergoing coagulation in the free-molecule regime, the time to reach the self-similar distribution is (Landgrebe & Pratsinis 1990; Vemury, Kusters & Pratsinis 1994)

$$\tau_{SP} = \frac{\tau_f}{A_1 v_o^{1/6} N_0}, \tag{2.11}$$

where $\tau_f \approx 5$ (Vemury *et al.* 1994), v_o is the initial particle volume, and N_0 is the initial particle concentration.

Using (2.3*a–d*) and the non-dimensional variables

$$n^* = \frac{n}{n_o}, \quad v^* = \frac{v}{v_o}, \tag{2.12a,b}$$

where n_o, v_o are the number density and volume of particles at the inlet, respectively, and substituting into (2.4), we obtain

$$\frac{\partial n^*}{\partial t^*} + u_j^* \frac{\partial n^*}{\partial x_j^*} = \frac{1}{Sc}\frac{1}{Re}\frac{\partial^2 n^*}{\partial x_j^* \partial x_j^*} + Da_{coag}\left(\frac{1}{2}\int_0^{v^*} \beta^*(w^*, v^*-w^*)\, n^*(w^*)\, n^*(v^*-w^*)\, \mathrm{d}w^* - \int_0^\infty \beta^*(v^*, w^*)\, n^*(v^*)\, n^*(w^*)\, \mathrm{d}w^*\right), \tag{2.13}$$

where $\beta^*(v^*, w^*) = (1/v^* + 1/w^*)^{1/2}(v^{*1/3} + w^{*1/3})^2$ is the normalised collision function, and $Sc = \nu/D_p$ is the particle Schmidt number (defined as the ratio of the kinematic viscosity to the particle diffusion coefficient). The factor Da_{coag} is the coagulation Damköhler number, which is equal to the ratio of a convection time scale

to a coagulation time scale. The time scales are defined here as in Garrick *et al.* (2006), and for the case of the free-molecule regime, Da_{coag} is given by

$$Da_{coag} = \frac{\tau_{conv}}{\tau_{coag}} = \frac{A_1 h N_0}{U_o} v_o^{1/6}, \tag{2.14}$$

where the convection time scale is $\tau_{conv} = h/U_o$, and the coagulation time scale is $\tau_{coag} = (A_1 N_0 v_o^{1/6})^{-1}$. For the case of an initially monodisperse aerosol, (2.11) shows that the coagulation time scale is one-fifth of the time needed to reach the self-preserving distribution. Based on (2.11) and (2.14), the coagulation Damköhler number can be written as

$$Da_{coag} = \frac{5\tau_{conv}}{\tau_{SP}}. \tag{2.15}$$

The assumptions of the approach adopted in the present paper are listed below.

(i) Coagulation in the free-molecule regime is considered, which means that particles should be smaller than the mean free path in the carrier fluid. It must be mentioned that our simulations are carried out in terms of dimensionless variables, but if we assume, for example, that the particles at the inlet of the jet have diameter 5 nm, then the maximum particle mean size in the jet would be around 25 nm, which is less than the mean free path in air at normal temperature and pressure (approximately 65 nm).

(ii) The particles have no effect on the fluid motion and do not affect the fluid properties (density, viscosity etc.). If we assume that the particles at the inlet have diameter 4–5 nm, the jet nozzle width is roughly 1 cm and the temperature of the jet is close to 50 °C, conditions not far from those in the experimental work of Junzong *et al.* (2013), then the particle volume fraction at the inlet is less than 10^{-6}. This value is small enough to ensure the validity of the assumption (Elghobashi 2006).

(iii) The particles are spherical due to instantaneous coagulation. While we are not considering a particular physical system, this is usually true for nanoparticle coagulation in the free-molecule regime.

(iv) The flow is assumed to be isothermal.

(v) Electrostatic effects (Van der Waals forces) are not taken into account.

(vi) The Stokes number St – which is the ratio of a characteristic time scale of the particles, $\tau_p = \rho_p d_p^2/(18\mu)$ (Friedlander 2000), to that of the flow, τ_f – is much smaller than unity and therefore the particles follow the fluid. This assumption is satisfied easily for nanoparticles, and an example is given here to justify this assertion. If we assume that particles at the inlet have diameter 5 nm, then the largest particles found in the jet (at the right edge of the PSD with very low number density) would have diameter 200 nm (as will be found later in this study). Then τ_p can be calculated by using $\rho_p = 2200\,\mathrm{kg\,m^{-3}}$, which is a typical value of density for silica nanoparticles, and $\mu = 1.82 \times 10^{-5}$. The smallest time scale in our problem is the Kolmogorov time scale, $\tau_\eta = \sqrt{\nu/\epsilon}$, and this is taken as τ_f in this example. The smallest non-dimensional value of τ_η calculated by the present DNS was 0.38, while the way the variables are non-dimensionalised has been shown in (2.3*a–d*). If we assume a jet nozzle width $h \approx 1$ cm, then the corresponding dimensional value of τ_η would be 7.59×10^{-4}. Based on these assumptions, the estimated Stokes number would be $St \approx 4 \times 10^{-4} \ll 1$.

(vii) A Schmidt number $Sc = 1$ is assumed for all particle classes. In reality, Sc takes a range of values because it depends on the particle diffusion coefficient D_p, which

in turn is a function of particle size according to the Stokes–Einstein equation (Friedlander 2000). For temperature 298 K, for example, particles with 20 nm diameter have Schmidt number 1415. The use of $Sc = 1$ implies higher diffusive transport, and studies of flows with high Sc have so far been conducted only in the context of 2-D flows, such as the study of Garrick & Khakpour (2004) on a 2-D mixing layer and the study of Cifuentes *et al.* (2020) on a 2-D flame–vortex interaction. However, a high Sc results in Batchelor scales, $\eta_c = \eta/\sqrt{Sc}$, that are much smaller than the Kolmogorov scale, η (Davidson 2004). For example, for $Sc = 1415$, η_c would be roughly 37 times smaller than η, hence in a 3-D flow, it would require a grid with 37^3 more cells. For the present simulation, which currently uses 52 million cells, this would amount to 2.6 trillion cells. Therefore, the study of the effect of high Sc in a 3-D flow simulation has to be left for future work.

2.2. *Numerical method*

The simulations were performed with our computational fluid dynamics (CFD) code, PANTARHEI, which is coupled with the in-house code for population balance modelling, CPMOD. PANTARHEI has been used to simulate a number of transitional and turbulent flows (Xiao & Papadakis 2019; Alves Portela, Papadakis & Vassilicos 2020). The incompressible Navier–Stokes equations are discretised by applying the finite volume method in unstructured grids, and all unknown variables are stored at the cell centroids (collocated variable arrangement). A second-order central discretisation scheme is employed for the convection and viscous terms, while a third-order backward differentiation formula (BDF) is used for the transient term. The orthogonal viscous terms are treated implicitly, while the convection term and the non-orthogonal diffusion terms are extrapolated from the previous three time steps. The pressure–velocity coupling is dealt with by the fractional step method. The code is parallelised with the aid of the PETSc and HYPRE libraries (Balay *et al.* 2021).

A method developed recently by Liu & Rigopoulos (2019) is employed for the discretisation of the PBE. The method (*a*) provides an accurate prediction of the distribution with a small number of sections, (*b*) conserves the first moment (or any other single moment) in coagulation, (*c*) is applicable to any non-uniform grid (even an adaptive one), and (*d*) is efficient and robust when coupled with CFD. It is based on the framework of finite-volume methods applied to the particle volume domain, v, truncated to (v_o, v_{max}). The latter is discretised in $(v_o, \ldots, v_k)$, the intervals $\Delta v_i = v_i - v_{i-1}$, $i = 1, \ldots, k$ are defined, and each interval corresponds to a number density n_i. One of the main challenges in the numerical solution of the PBE is the conservation of the first moment in coagulation, due to the presence of the integral terms. In our method, a transformation is employed to decompose the birth term into fluxes of coagulating particles, and a map is constructed to record them. An algorithm for constructing this map in an arbitrary non-uniform grid has been developed, and the aggregation birth and death terms are then calculated via these fluxes, resulting in mass conservation without introducing correction terms. The map is constructed once at the start of the simulation and accessed throughout the run, making the method computationally efficient and easy to couple with CFD. Test cases, including analytical solutions and a co-flow laminar flame (Liu & Rigopoulos 2019), have shown that the method produces very accurate solutions that conserve the first moment, even on coarse grids.

After discretisation in the volume domain, the PBE is converted into a coupled system of partial differential equations that govern the temporal and spatial evolution of the PSD

in terms of discretised number densities, n_i. The transport equation for n_i is

$$\frac{\partial n_i}{\partial t} + \frac{\partial (u_j n_i)}{\partial x_j} = \frac{\partial}{\partial x_j}\left(D_p \frac{\partial n_i}{\partial x_j}\right) + S_i(n_1, \ldots, n_k), \tag{2.16}$$

where the source term, $S_i(n_1, \ldots, n_k)$, represents the effect of coagulation for particles in the interval i. The numerical scheme used for the solution of these transport equations is slightly different from that described previously for the flow field. More specifically, the convection and viscous terms are treated explicitly using third-order extrapolation from the previous three time steps. The values of $n_1, \ldots, n_k$ are also extrapolated similarly and used to calculate S_i. In order to ensure boundedness for n_i, the Gamma differencing scheme (Jasak, Weller & Gosman 1999) was employed for the discretisation of the convection term, and the value 0.1 was used for the scheme parameter β_m.

2.3. *Flow configuration and computational setup*

Direct numerical simulations of a 3-D spatially developing planar turbulent jet were performed. The jet is laden with monodisperse nanoparticles and flows into a particle-free co-flow stream. There is a wealth of data for validating the flow field (Rajaratnam 1976; Le Ribault, Sarkar & Stanley 1999; Pope 2000; Stanley, Sarkar & Mellado González 2002; Klein, Sadiki & Janicka 2003*a*,*b*; Suresh *et al.* 2008; Watanabe *et al.* 2014).

The flow configuration is similar to that of Stanley *et al.* (2002). The Reynolds number is $Re = U_o h/\nu = 3000$, and the ratio of co-flow velocity, U_∞, to the jet velocity, U_o, is $U_\infty/U_o = 0.2$. The x, y and z coordinates (corresponding to indices $i = 1, 2, 3$ in the notation of (2.1)) are defined in the streamwise, cross-stream and spanwise directions, respectively. Turbulent properties are statistically homogeneous in the z direction. The size of the computational domain $L_x \times L_y \times L_z$ is $25h \times 26h \times 5h$, similar to that of Stanley *et al.* (2002) and Das & Garrick (2010). The computational domain is long enough in the streamwise direction for the flow to reach fully developed turbulence. In addition, the domain is extended in the cross-stream direction in order to minimise the effect of the top and bottom boundaries.

A convective boundary condition was applied at the outlet boundary in the streamwise direction; this boundary condition allows vortices to propagate through the exit plane with minimal reflection. Periodic boundary conditions were used in the spanwise direction. Finally, a symmetry boundary condition was applied in the top and bottom boundaries. This condition does not allow for mass entrainment, and this causes a small reduction in the local co-flow velocity in the streamwise direction. To mitigate this effect, the computational domain was significantly extended in the cross-stream direction. Good agreement between the DNS and reference data from the literature, to be presented later, in § 3.1, suggests that the effect of the boundaries is very small.

At inflow, a top-hat profile with smooth edges is prescribed for the mean (i.e. time-averaged) velocity. The profile is given by (Klein *et al.* 2003*b*; Stanley *et al.* 2002)

$$\overline{U}(y) = \frac{U_o + U_\infty}{2} + \frac{U_o - U_\infty}{2} \tanh \frac{-|y| + h/2}{2\theta_o}, \tag{2.17}$$

where $\theta_o = h/20$ (Le Ribault *et al.* 1999) is the shear layer momentum thickness. The mean cross-stream and spanwise velocities were set to zero. The mean profile of the

number density for the first interval n_1 is given by the tangential profile

$$\overline{n_1}(y) = n_{1o} + n_{1o} \tanh \frac{-|y| + h/2}{2\theta_o}, \tag{2.18}$$

where n_{1o} is the time-averaged value of n_1 at the centreline.

The method of Klein *et al.* (2003*a*) was employed to generate artificial turbulent fluctuations at the inlet. The method requires a mean velocity profile, a profile for the Reynolds stresses, turbulence length and time scales, a filter width, and the number of slices (snapshots) of data to be generated. The output of the algorithm is a 3-D matrix that represents the velocity components at the inlet plane for different time snapshots. In the present study, the mean velocity profile is given by (2.17). Strictly speaking, the r.m.s. profile in the x direction, u_{rms}, should be zero at $y = \pm h/2$. However, it grows quickly due to high shear, and for this reason, u_{rms}/U_o is set to 1.25 % at the jet centreline, and increases parabolically to 5 % at $y = \pm h/2$. The turbulence intensity of the co-flow is set to 1 %. This u_{rms} profile is similar to that employed by Stanley *et al.* (2002). The velocity r.m.s. profiles in the y and z directions were set equal to u_{rms}. The turbulence length scale was $l_{Turb} = 0.3h$, and the turbulence time scale was $t_{Turb} = 10h/U_o$, where it was assumed that $t_{Turb} = l_{Turb}/U_{rms}$, with $U_{rms} = 3\,\%U_o$. A discussion on the value and the effect of the turbulence length scale can be found in Klein *et al.* (2003*a*). The number of snapshots was equal to 100, which is large enough to generate data for one flow-through time (defined using the length of the computational domain and the co-flow velocity, $T = L_x/U_\infty$). The number of snapshots was calculated based on the prescribed turbulence length and time scales mentioned above.

The simulations were performed on a non-uniform computational grid with approximately 52 million cells, distributed as $900 \times 452 \times 128$ in the x, y, z directions, respectively. The grid spacing was uniform in the x and z directions, and equal to $\Delta x = 0.028h$ and $\Delta z = 0.039h$. In the y direction, it was very fine close to the centreline, where $\Delta y = 0.018h$, and increased exponentially towards the boundaries, where $\Delta y = 0.124h$. The time step was $\Delta t = 0.005h/U_o$, resulting in a maximum Courant–Friedrichs–Lewy (CFL) number of 0.24. Convergence studies with a perfectly stirred reactor showed that this time step is adequate for the coagulation dynamics for the conditions considered.

Each simulation was run first for one flow-through time T to reach a state that is independent of the initial conditions (recall that T is defined using the co-flow velocity U_∞, which is five times smaller than U_o). Following this, the simulations were run for 80 000 time steps (corresponding to $3.2T$), and statistics were computed by averaging in time and in the homogeneous spanwise direction. Finally, where possible, exploitation of the jet symmetry with respect to the centreline was used to double the sample size. The number of cores was 1008, and 84 672 Cray XC30 CPU hours were required for each case.

The maximum value of the ratio of cell size, defined as $\Delta_{cell} = (\Delta x\,\Delta y\,\Delta z)^{1/3}$, to the Kolmogorov length scale $\eta = (\nu^3/\epsilon)^{1/4}$ in the domain was 2.8, while the mean value in the region of fully developed turbulence was 1.95. The grid resolution was assessed by checking the balance of the turbulent kinetic energy equation; results are shown in Appendix A, figure 17. The terms of the equation balance well, and the maximum error was less than 5.5 % of the peak absolute value of convection due to mean flow, indicating that the grid resolution is fine enough. The one-dimensional spectra of the velocity fluctuations for a selected point in the fully turbulent region are also presented in Appendix A, figure 18. The spectra exhibit a $-5/3$ power-law slope over about a decade. There is also a dissipative range with faster decay rate at high frequencies,

	Da_{coag}	Re	PSD becomes self-preserving	No. of intervals	v_{max}/v_o
Case 1	1	3000	before jet break-up	35	11 250
Case 2	$\frac{1}{3}$	3000	after jet break-up	35	2800

Table 1. Computational parameters of the simulations.

indicating that the turbulent motions are well resolved. The maximum Reynolds number $Re_\lambda = \sqrt{\overline{|\boldsymbol{u}'|^2}}\lambda/\nu$, based on the Taylor micro-scale $\lambda = \sqrt{\nu\overline{|\boldsymbol{u}'|^2}/\epsilon}$, was found to be 160.

Simulations for two different coagulation Damköhler numbers, $Da_{coag} = 1$ and $Da_{coag} = 1/3$, were performed. The values of Da_{coag} are close to those examined in previous studies of nanoparticle coagulation (Garrick *et al.* 2006; Garrick 2011). The two cases correspond to different times for the PSD to reach the self-preserving distribution. According to (2.15), in a perfectly stirred reactor, these times would be $\tau_{SP} = 5$ and $\tau_{SP} = 15$, respectively. As will be shown later, the jet breaks up at $x/h \approx 7.5$. For the chosen values of Da_{coag}, the PSD becomes self-similar upstream and downstream of the break-up location for the first and second cases, respectively.

The PBE was discretised with 35 intervals in the particle volume domain. An exponential grid was employed for all cases; this is well suited for fast-growing particles. The range $(v_o, \ldots, v_{max})$ covered was different for each Da_{coag} case; v_o remained the same but the maximum value was $v_{max} = 11\,250v_o$ for $Da_{coag} = 1$, and $v_{max} = 2800v_o$ for $Da_{coag} = 1/3$. Convergence studies with a perfectly stirred reactor showed that this grid is sufficiently accurate and ensures that the size distribution does not grow beyond the maximum value during the simulation time. The computational parameters of the simulations are also summarised in table 1.

The simulations were carried out in terms of dimensionless variables. The non-dimensionalisation of the equations is described in § 2.1, where an asterisk was introduced to denote dimensionless variables; refer to (2.3*a–d*) and (2.12*a*,*b*). In the sections that follow, only dimensionless variables are presented, and for the sake of simplicity, the asterisk has been removed.

3. Comparison with reference data

3.1. *Flow field*

In this section, the DNS data for the planar jet flow are presented and compared with experimental and other reference simulation data from the literature. Additional data for the balance of the terms in the turbulent kinetic energy equation and the one-dimensional spectra of turbulent fluctuations are given in Appendix A. The turbulent kinetic energy, k, in the $(x$–$y)$ plane is depicted in figure 1(*a*) (because of symmetry, only the top half is shown). The jet breaks up at $x \approx 7.5$, and downstream of this location the turbulent kinetic energy rapidly grows and decays again; the maximum of k is located at $(x, y) = (11, 0.7)$. Contours of instantaneous spanwise vorticity and passive scalar fields, ω_z and ϕ, are shown in figures 1(*b*) and 1(*c*), respectively. A downstream region with intense turbulent mixing and a wide range of turbulence length scales is evident.

The growth of the jet half-width based on the streamwise velocity, δ_U, is shown in figure 2(*a*). The jet half-width δ_U is defined as the distance from the symmetry plane (centreline) to the point in the cross-stream direction where the mean streamwise velocity

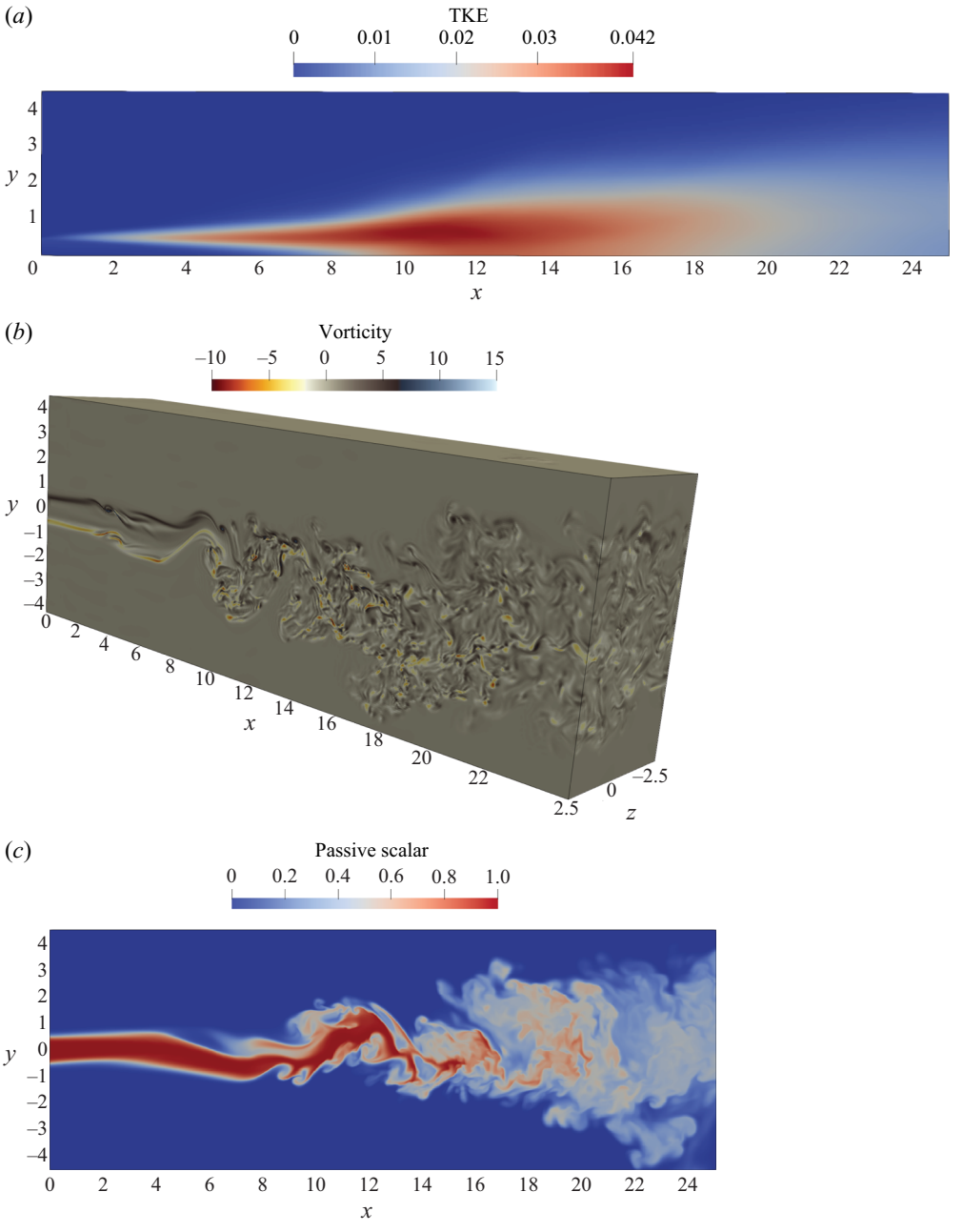

Figure 1. Flow field data: (*a*) turbulent kinetic energy (TKE) k; (*b*) 3-D view of the instantaneous spanwise vorticity field ω_z; (*c*) instantaneous contours of the passive scalar on (x–y) plane $z = 0$.

excess with respect to the co-flow velocity, $U_e(x, y) = U(x, y) - U_\infty(x)$, is half that with respect to the centreline, $\Delta U_c(x) = U_c(x) - U_\infty(x)$. The ratio of the velocity excess at the jet nozzle exit, $\Delta U_o = U_o - U_\infty$, to $\Delta U_c(x)$ is shown in figure 2(*b*).

The growth of the jet half-width based on the passive scalar, δ_ϕ, is shown in figure 3(*a*). The half-width δ_ϕ is defined (similarly to δ_U) as the distance from the symmetry plane

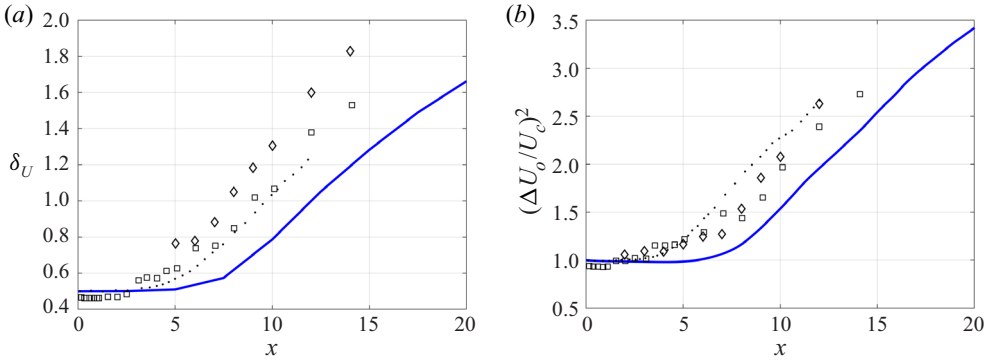

Figure 2. Growth of the jet half-width based on the velocity (*a*) and centreline mean velocity excess decay (*b*). Blue line, present results; □, Thomas & Chu (1989); ◇, Browne *et al.* (1983); dotted line, DNS (Stanley *et al.* 2002).

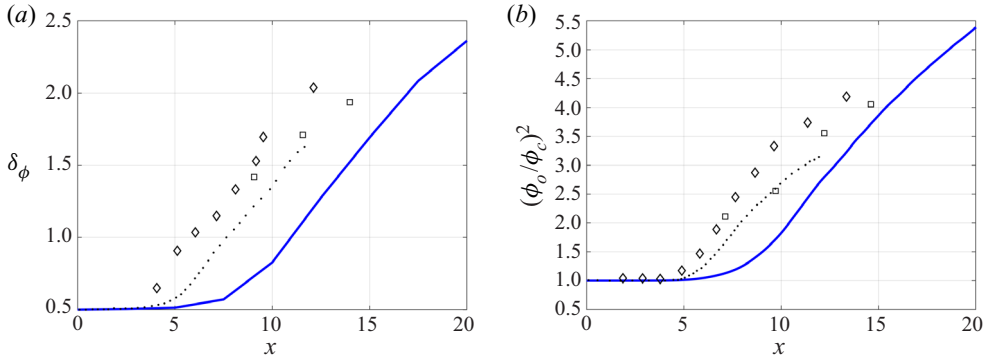

Figure 3. Downstream growth of the jet half-width based on the passive scalar (*a*) and decay of the mean scalar on the jet centreline (*b*). Blue line, present results; ◇, Browne *et al.* (1983); □, Davies, Keffer & Baines (1975); dotted line, DNS (Stanley *et al.* 2002).

(centreline) to the point where the passive scalar concentration is half of that on the centreline. The mean scalar decay, defined as $(\phi_o/\phi_c)^2$, where $\phi_c(x)$ is the value at the centreline and ϕ_o is the value at the jet nozzle exit, is shown in figure 3(*b*).

It can be seen that there is good agreement with the experimental and other reference data. Theoretical analysis (Rajaratnam 1976; Pope 2000) suggests that $\delta_U \propto x$ and $U_c \propto 1/\sqrt{x}$ for planar jet flow, and the same scaling is also valid for the scalar concentration. It has been documented (Stanley & Sarkar 2000; Stanley *et al.* 2002; da Silva, Lopes & Raman 2015) that the jet break-up location is highly affected by the inlet conditions at the nozzle. The jet characteristics are also affected by the value of the Reynolds number in cases where $Re < 10\,000$ (Klein *et al.* 2003*b*; Deo, Mi & Nathan 2008). Therefore, independently of the exact location of the jet break-up, the slope of the curves shown in figures 2 and 3 for the present DNS exhibits good agreement with that of reference data.

The self-similar cross-stream profiles for velocity and scalar are depicted in figures 4(*a*) and 4(*b*), respectively. The velocity profiles collapse to a single curve, and there is good agreement with reference (experimental or other DNS) data. The velocity field reaches self-similarity at $x \approx 12$, while the passive scalar is slightly slower to develop and the

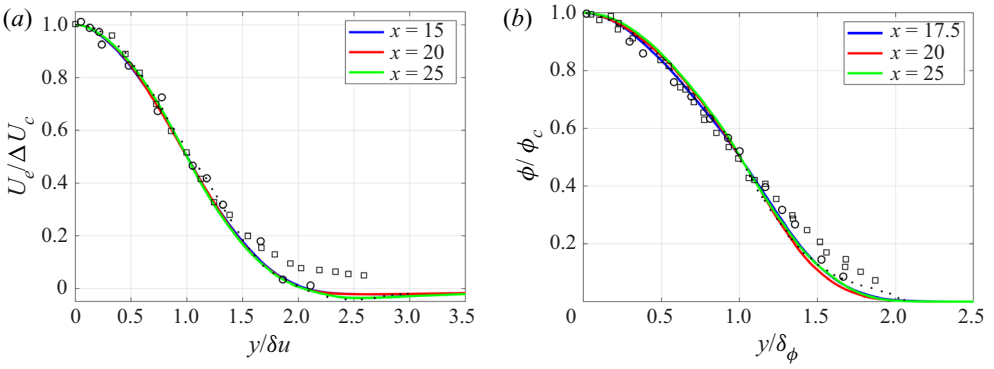

Figure 4. Self-similar profiles of mean velocity and mean passive scalar for three axial positions. (*a*) Mean velocity: solid lines, present results; □, Gutmark & Wygnanski (1976); ○, Ramaprian & Chandrasekhara (1985); dotted line, DNS (Stanley *et al.* 2002). (*b*) Mean scalar: solid lines, present results; □, Davies *et al.* (1975); ○, Jenkins & Goldschmidt (1973); dotted line, DNS (Stanley *et al.* 2002).

self-similar region is reached at $x \approx 17$. The same behaviour was also observed by Stanley *et al.* (2002).

3.2. *Particle size distribution*

The DNS–PBE approach allows for the prediction of the PSD at every point in the domain. As mentioned in § 2.1, in a perfectly stirred reactor, the PSD reaches a self-preserving distribution. Figure 5 shows the time-averaged PSDs at five different probe points on the centreline for both Da_{coag} number cases. The computed distributions are scaled according to (2.9) and (2.10), and compared with the self-preserving PSD from Vemury & Pratsinis (1995). It can be seen that as the PSDs develop, they approach the self-preserving distribution and there is good agreement with the reference data, especially close to the exit of the domain. Turbulence may affect the time to reach the self-preserving state (Friedlander 2000). As mentioned earlier, the values of Da_{coag} were chosen in such a way that the PSD becomes self-preserving before and after the jet break-up location for the two cases. In particular, for the $Da_{coag} = 1/3$ case, the PSD becomes self-preserving slightly downstream of the expected location ($x \approx 15$). However, the difference observed is small. The fact that the PSDs in the turbulent flow field do not deviate a lot from the self-preserving distribution can be attributed to the lack of recirculating flow structures that would bring into contact particles with different distributions and would make the PSD deviate from the self-preserving state. Finally, the good matching with the reference data indicates that the number and distribution of volume intervals are sufficient to resolve the PSD accurately.

4. Results and discussion

4.1. *Effect of coagulation and mixing on the moments*

The evolution of the moments is dominated by two physical mechanisms, coagulation and turbulent mixing, and by their interaction. Coagulation reduces the total number of particles, M_0, with increasing distance from the orifice, but it does not alter the total particle volume, M_1, which behaves as a passive scalar. It also brings about an increase

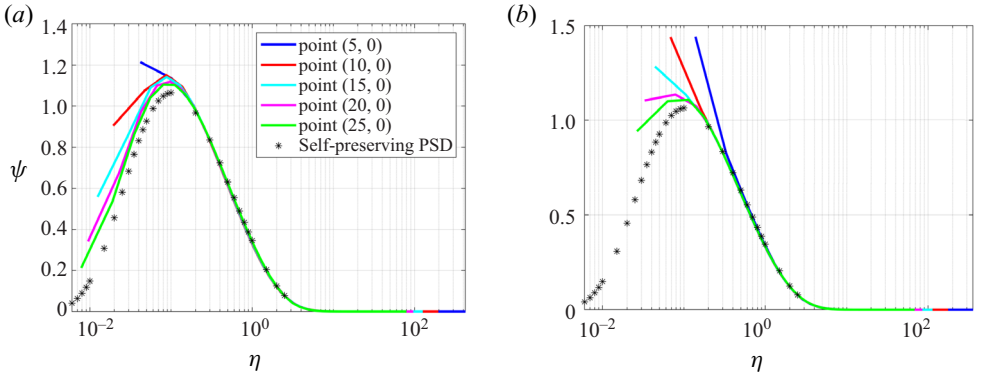

Figure 5. Normalised time-averaged PSDs at several probe points along the centreline. The results are compared with reference data for the self-preserving distribution (Vemury & Pratsinis 1995). A logarithmic scale was used for the horizontal axes. (*a*) $Da_{coag} = 1$; (*b*) $Da_{coag} = 1/3$.

in the second moment, M_2, due to the heavier weighting of the large particles on the distribution. Turbulent mixing brings about dilution, which can be quantified using M_1.

The instantaneous M_0 fields for the two Da_{coag} cases are depicted in figures 6(*a*) and 6(*b*), while the instantaneous M_2 fields are shown in figures 7(*a*) and 7(*b*). It is evident that M_0 reduces at downstream locations. The second moment, M_2, attains small values close to the jet nozzle and increases rapidly due to coagulation until the jet break-up location. The jet becomes unstable and breaks into smaller vortices, while the entrainment of co-flow fluid dilutes the large values of M_2. However, as can be seen, for example, in figure 7(*a*), the remnants of the core of the jet (see region $14 < x < 22$) are fluid patches with large values of M_2. Further downstream, the small-scale motion due to the strong turbulence in the jet has mixed further the fluid patches of the jet core. However, it is evident that M_0 reduces quite fast, while fluid patches with large values of M_2 start to emerge.

The evolution of the zeroth moment, M_0, is governed by the following equation in non-dimensional form, derived from (2.8) for $k = 0$:

$$\frac{\partial M_0}{\partial t} + u_j \frac{\partial M_0}{\partial x_j} = \frac{1}{Sc}\frac{1}{Re}\frac{\partial^2 M_0}{\partial x_j \partial x_j} - \frac{1}{2} Da_{coag} \int_0^\infty \int_0^\infty \beta(v, w)\, n(v)\, n(w)\, \mathrm{d}v\, \mathrm{d}w. \quad (4.1)$$

The source term is negative because coagulation results in a reduction in the total number of particles. Figure 8(*a*) shows the centreline variation of the time-averaged $\overline{M_0}$, juxtaposed with $\overline{M_1}$. There is a rapid reduction of the particle number concentration close to the jet nozzle, and the rate is higher for the higher Da_{coag}; this is expected because higher Da_{coag} represents more intense coagulation. Both curves start to change behaviour at $x \approx 7.5$, where the jet breaks up and turbulent mixing starts to play an important role. From figure 8(*a*) it is evident that the rate of reduction (slope) of $\overline{M_0}$ is larger than that of $\overline{M_1}$ in the region of fully developed turbulence ($x > 15$). Dilutions due to turbulent mixing and coagulation work in unison and result in a reduction of M_0. The contribution of each mechanism can be quantified as follows. In the case of $Da_{coag} = 1$, $\overline{M_0}$ is reduced by 89 % between the jet break-up location and the exit of the domain, while a passive scalar, such as $\overline{M_1}$, is reduced by 58 %. Similarly, in the case of $Da_{coag} = 1/3$, $\overline{M_0}$ is reduced by 88 % between the same locations. This indicates that both effects contribute to the evolution of $\overline{M_0}$, with turbulent dilution (rather than coagulation) having a slightly stronger effect.

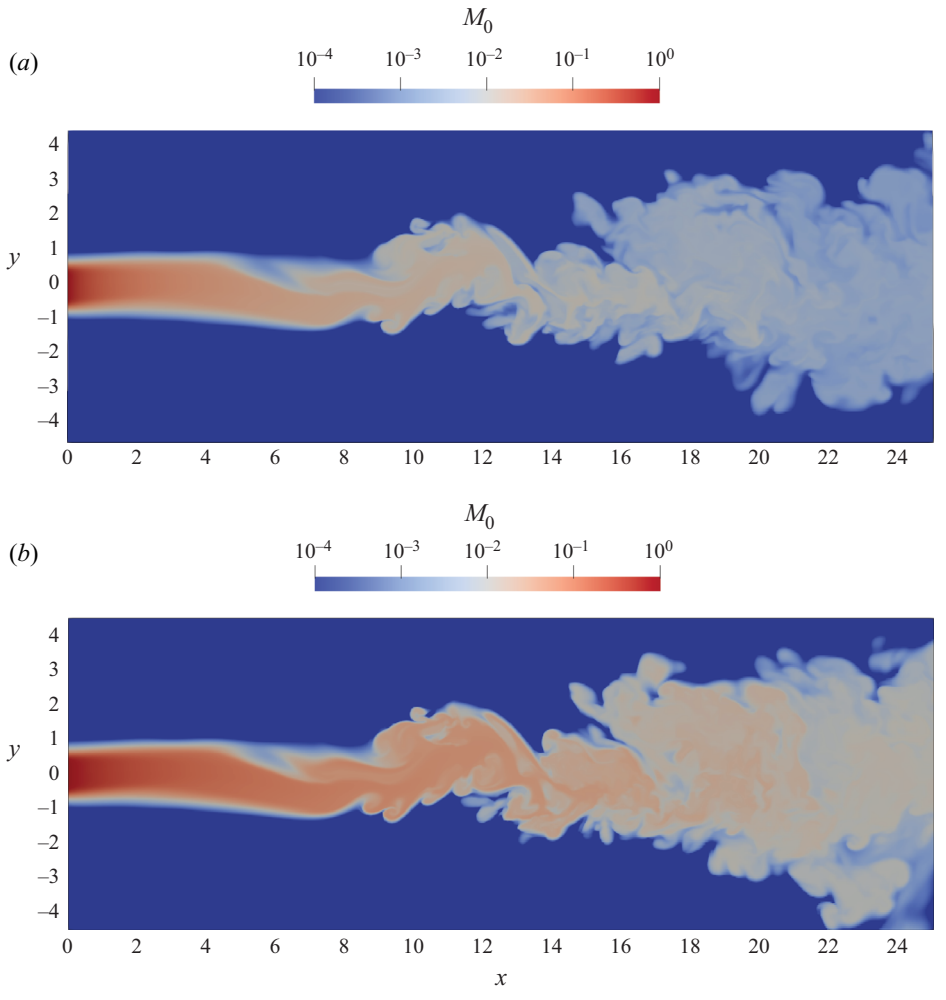

Figure 6. Instantaneous contour plots of M_0 on (x–y) plane $z = 0$. (*a*) $Da_{coag} = 1$; (*b*) $Da_{coag} = 1/3$. A logarithmic scale colourbar is used.

The transport equation for the second moment, M_2, is derived from (2.8) for $k = 2$:

$$\frac{\partial M_2}{\partial t} + u_j \frac{\partial M_2}{\partial x_j} = \frac{1}{Sc}\frac{1}{Re}\frac{\partial^2 M_2}{\partial x_j \partial x_j} + Da_{coag}\int_0^\infty \int_0^\infty vw\,\beta(v, w)\,n(v)\,n(w)\,\mathrm{d}v\,\mathrm{d}w. \quad (4.2)$$

For this moment, the source term is positive. Figure 8(*b*) shows the centreline variation of the time-averaged $\overline{M_2}$. Unlike M_0, in the case of M_2 there is competition between dilution and coagulation. Turbulent mixing acts towards reducing M_2, while coagulation acts towards increasing M_2. As can be seen in figure 8(*b*), the net result is an increase in M_2. The effect of turbulence is thus to mitigate the rapid growth of the second moment. The net increase of $\overline{M_2}$ with distance after the jet break-up location indicates that coagulation has a greater effect on the evolution of M_2 compared to dilution.

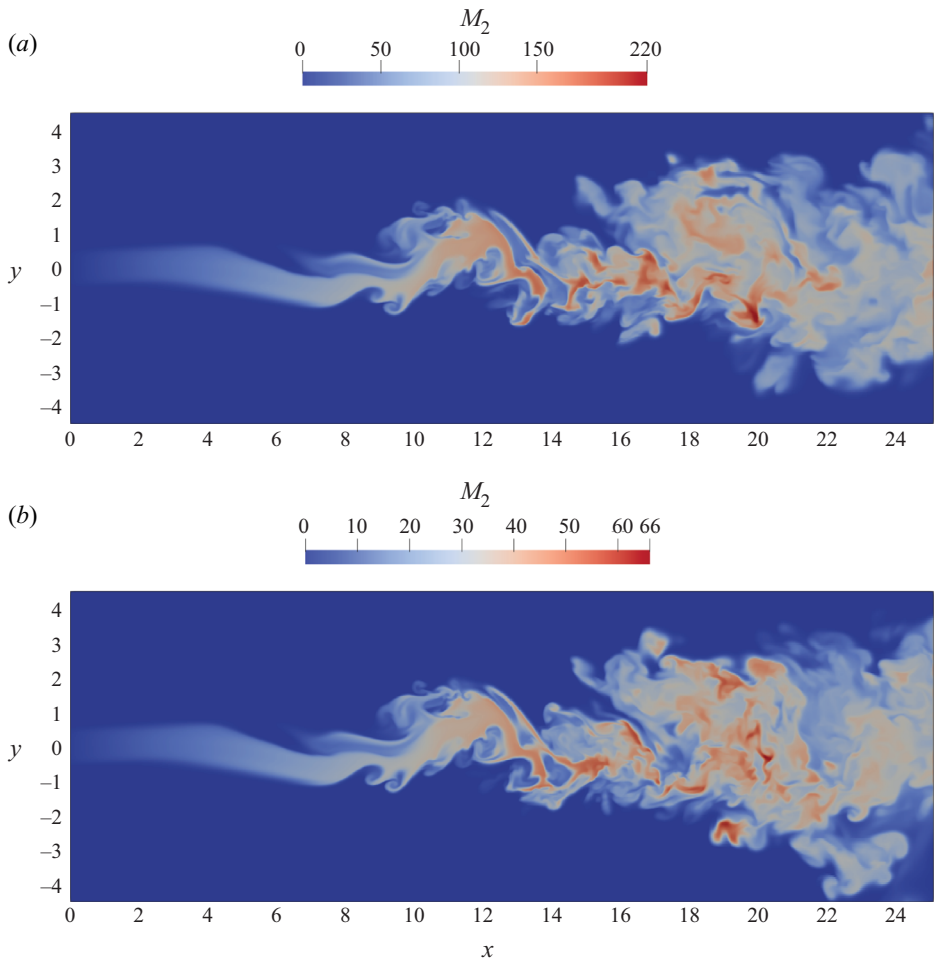

Figure 7. Instantaneous contour plots of M_2 on (x–y) plane $z = 0$.(*a*) $Da_{coag} = 1$; (*b*) $Da_{coag} = 1/3$.

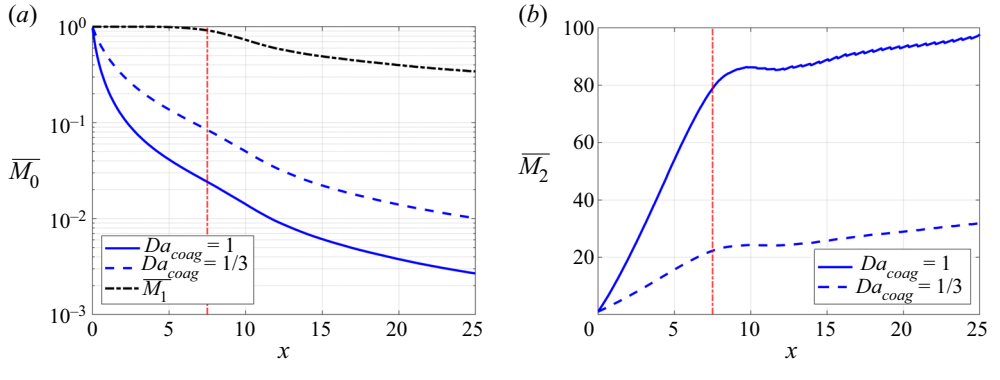

Figure 8. Centreline variation of time-averaged M_0 (*a*) and M_2 (*b*) for the two Da_{coag} cases. The red dashed-dotted line indicates the jet break-up location. A logarithmic scale was used for the vertical axis in (*a*). A black dashed-dotted line is used for $\overline{M_1}$ in (*a*).

4.2. *Coagulation source term correlations*

We now turn our attention to the effect of turbulent fluctuations and consider the Reynolds decomposition of the PBE (Scott 1967; Friedlander 2000; Rigopoulos 2007). Apart from velocities, the number densities are also decomposed into mean and fluctuating parts, and this decomposition is substituted into (2.4). Time-averaging results in the equation

$$\begin{aligned}\bar{u}_j \frac{\partial \bar{n}}{\partial x_j} + \frac{\partial \overline{u_j' n'}}{\partial x_j} &= \frac{1}{Sc}\frac{1}{Re}\frac{\partial^2 \bar{n}}{\partial x_j \partial x_j} \\ &+ Da_{coag}\left(\frac{1}{2}\int_0^v \beta(w, v-w)\,\bar{n}(w)\,\bar{n}(v-w)\,\mathrm{d}w - \int_0^\infty \beta(v, w)\,\bar{n}(v)\,\bar{n}(w)\,\mathrm{d}w\right. \\ &\left. + \frac{1}{2}\int_0^v \beta(w, v-w)\,\overline{n'(w)\,n'(v-w)}\,\mathrm{d}w - \int_0^\infty \beta(v, w)\,\overline{n'(v)\,n'(w)}\,\mathrm{d}w\right). \end{aligned} \tag{4.3}$$

The time-averaging of the transient term in (2.4) is zero for jet flow cases where statistical stationarity is reached. The last two terms arise due to turbulent coagulation; both involve integrals of correlations between number density fluctuations and are unclosed. Lack of understanding of the behaviour of correlations $\overline{n'(v)\,n'(w)}$ is a long-standing problem in the literature (Levin & Sedunov 1966, 1968; Scott 1967; Warshaw 1967; Drake 1972).

The Reynolds decomposition can also be applied to the transport equation of moments, (2.8), resulting in

$$\begin{aligned}\bar{u}_j \frac{\partial \overline{M_k}}{\partial x_j} + \frac{\partial \overline{u_j' M_k'}}{\partial x_j} &= \frac{1}{Sc}\frac{1}{Re}\frac{\partial^2 \overline{M_k}}{\partial x_j \partial x_j} \\ &+ Da_{coag}\left(\frac{1}{2}\int_0^\infty\int_0^\infty (v+w)^k\,\beta(v, w)\,\bar{n}(v)\,\bar{n}(w)\,\mathrm{d}v\,\mathrm{d}w\right. \\ &- \frac{1}{2}\int_0^\infty\int_0^\infty (v^k + w^k)\,\beta(v, w)\,\bar{n}(v)\,\bar{n}(w)\,\mathrm{d}v\,\mathrm{d}w \\ &+ \frac{1}{2}\int_0^\infty\int_0^\infty (v+w)^k\,\beta(v, w)\,\overline{n'(v)\,n'(w)}\,\mathrm{d}v\,\mathrm{d}w \\ &\left. - \frac{1}{2}\int_0^\infty\int_0^\infty (v^k + w^k)\,\beta(v, w)\,\overline{n'(v)\,n'(w)}\,\mathrm{d}v\,\mathrm{d}w\right). \end{aligned} \tag{4.4}$$

Similarly to the transport equation for the number density, the last two terms are unclosed. Analysis of these terms is important since the moments are measured frequently in experiments, and also a family of numerical methods for modelling particulate flows is based on the method of moments. Our analysis will focus on the unclosed terms in the transport equations of $\overline{M_0}$ and $\overline{M_2}$ (coagulation does not alter $\overline{M_1}$, as already mentioned). Knowledge of these moments is also required in order to characterise the particle field with the method of moments when a log-normal size distribution is assumed (Brock, Kuhn & Zehavi 1986).

As was mentioned in § 2.3, 35 intervals Δv_i were used to discretise the particle volume space v, thus for each computational cell there are 35×35 correlations $\overline{n_i' n_j'}$. As this is a very large amount of information, maps are presented for only a few points of interest in the domain. Results for the number density fluctuation correlations $\overline{n'(v)\,n'(w)}$ for the two values of Da_{coag} at points $(x, y, z) = (10, 0, 0)$ and $(17.5, 0.5, 0)$ are shown in

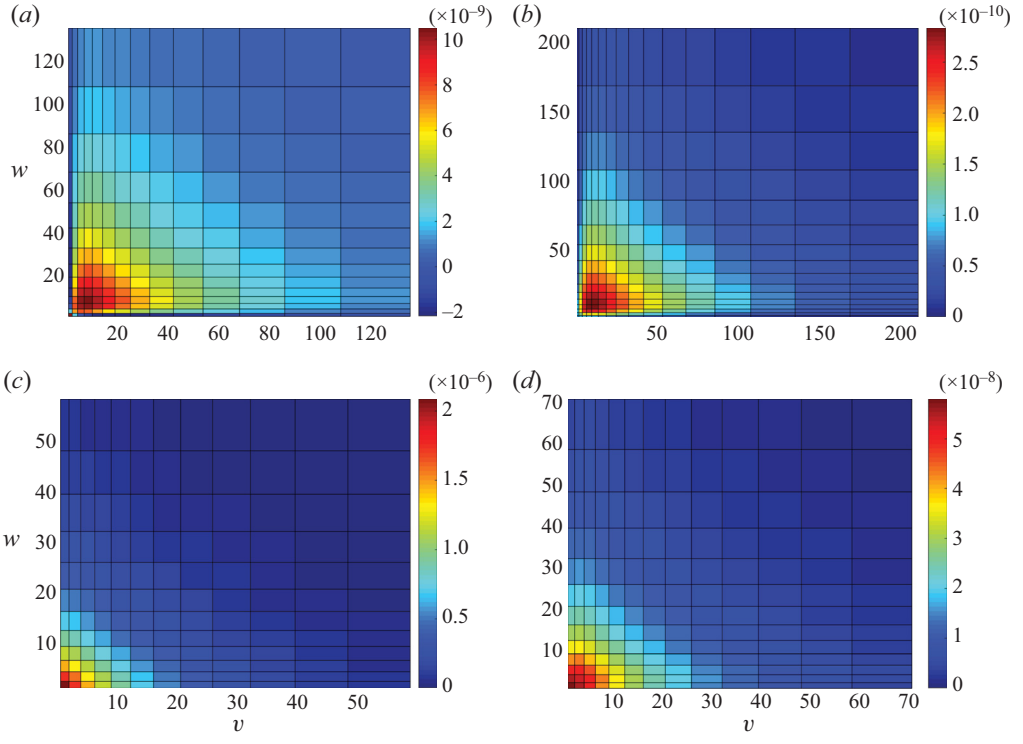

Figure 9. Map of number density fluctuation correlations $\overline{n'(v)\,n'(w)}$: (*a*) for $Da_{coag} = 1$ at probe point (10, 0, 0); (*b*) for $Da_{coag} = 1$ at probe point (17.5, 0.5, 0); (*c*) for $Da_{coag} = 1/3$ at probe point (10, 0, 0); (*d*) for $Da_{coag} = 1/3$ at probe point (17.5, 0.5, 0).

figure 9. The first point is located on the centreline and relatively close to the jet break-up location ($x \approx 7.5$), while the second point is further downstream, in the region of fully developed turbulence and slightly off the centreline. The results are presented in the form of contour maps with non-uniform spacing because of the exponential grid employed for the discretisation of the particle volume space. The map of the time-averaged number density combinations $\overline{n(v)}\,\overline{n(w)}$ for $Da_{coag} = 1$ at probe point (10, 0, 0) is also shown in figure 10(*a*). As expected, the maps are symmetric with respect to the diagonal $v = w$. For most of the points examined, it is found that the magnitude of $\overline{n'(v)\,n'(w)}$ follows that of $\overline{n(v)}\,\overline{n(w)}$, as can be seen in figures 9(*a*) and 10(*a*). More specifically, the maximum value of the correlation is found along the diagonal $v = w$ and close to the interval where $\bar{n}(v)$ has a local maximum, which is at the same interval where $\overline{n(v)}\,\overline{n(w)}$ receives the maximum value. For instance, the PSD at probe point (10, 0, 0) for $Da_{coag} = 1$, shown in figure 10(*b*), has a local maximum for $v \approx 5$ (in terms of discretised PBE, this corresponds to the third interval, $\overline{n_3}$), while the maximum value of the correlations at the same probe point were found for $(v, w) \approx (7.1, 7.1)$ (see figure 10*a*). Furthermore, for large values of v and w, $\overline{n'(v)\,n'(w)}$ tends to zero. These values correspond to the right tail of the PSD, where the mean number density $\bar{n}(v)$ is small (there are few particles of large size, as seen in figure 10*b*).

The correlations $\overline{n'(v)\,n'(w)}$ are found to be mostly positive for most v, w combinations, as shown in figure 9. Since we are not considering differential diffusion of particles of different sizes, the distribution is affected as a whole by turbulence, and coagulation is not

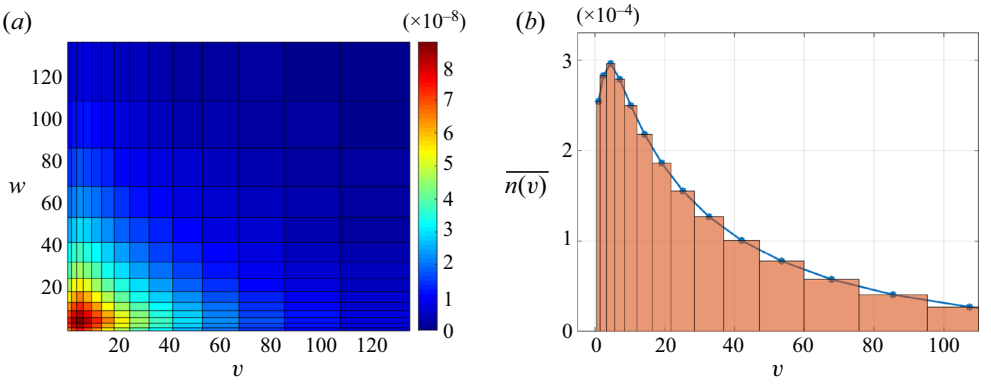

Figure 10. (*a*) Map of time-averaged number density combinations $\overline{n(v)}\,\overline{n(w)}$; (*b*) time-averaged PSD for $Da_{coag} = 1$ at probe point (10, 0, 0).

rapid enough to redistribute fluctuations in a way that generates negative correlations, with the exception discussed below.

Negative values of the correlations $\overline{n'(v)\,n'(w)}$ can also appear. This can be seen, for example, in figure 9(*a*) for $Da_{coag} = 1$ at probe point (10, 0, 0). These negative values involve mainly the fluctuation of the number density of the first interval, n_1', and that of intervals that are on and to the right of the local maximum of $\bar{n}(v)$ (see figure 10*b*), e.g. the correlations $\overline{n_1'\,n_3'}$ and $\overline{n_1'\,n_4'}$ etc. A possible explanation for this effect is that at the inlet, only n_1 is non-zero, and coagulation acts towards reducing the instantaneous values of n_1 and increasing those of n_2, n_3, etc. A general trend is that the effect of coagulation is to move the distribution to the right in particle volume space towards higher particle volumes. For example, at probe point (10, 0, 0), on average, coagulation acts towards reducing the instantaneous values of n_1 and increasing those of intervals at the right of the local maximum of $\bar{n}(v)$, such as n_4 (see figure 10*b*). Therefore, negative fluctuations of n_1', in that case, are correlated with positive fluctuations of n_4' and vice versa (when n_1 is consumed, n_4 is created). Once coagulation has progressed and the consumption of n_1 is not so intense, the correlations become positive. This also partly explains why negative correlations are found only for the case of intense coagulation ($Da_{coag} = 1$) and for points close to the jet break-up location ($x < 12.5$). Data for the downstream location (17.5, 0.5, 0) are presented in figure 9(*b*), and it is observed that $\overline{n'(v)\,n'(w)} > 0$ for all combinations of (v, w). Negative correlations are not found for the case $Da_{coag} = 1/3$ (see also figures 9*c*,*d*). This means that n_1' and n_i' have the same sign probably because of the increased effect of turbulent mixing compared to the effect of coagulation.

It is of interest to examine the value of $\overline{n'(v)\,n'(w)}$ in relation to the value of $\overline{n(v)\,n(w)}$. The intensity of the correlations of the number density fluctuations, the square of the passive scalar fluctuation intensity and the turbulence intensity are defined, respectively, as

$$I_n = \frac{\overline{n'(v)\,n'(w)}}{\overline{n(v)\,n(w)}}, \quad I_\phi = \frac{\overline{\phi'^2}}{\overline{\phi^2}}, \quad I_u = \frac{\overline{u_i'^2}}{\overline{U_i^2}}, \tag{4.5a–c}$$

where I_u is defined here for future reference. Figure 11 shows a surface plot of I_n at the probe point (10, 0, 0) for the two Da_{coag} cases. Here, I_n is normalised with the value of I_ϕ at that specific location, while the location where the fluctuation intensities are equal

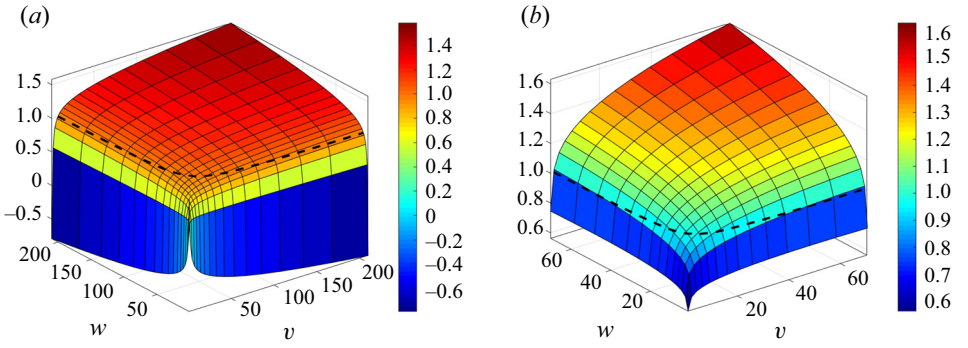

Figure 11. Intensity of correlations of number density fluctuations I_n at probe point (10, 0, 0): (*a*) $Da_{coag} = 1$; (*b*) $Da_{coag} = 1/3$. Results are normalised by $I_\phi = 0.156$. The black dashed line indicates the location where the fluctuation intensities are equal, i.e. $I_n = I_\phi$.

($I_n = I_\phi$) is also shown. First, note that the negative correlations referred to above can be seen very clearly in this plot. The differences with I_ϕ are small for the combinations (v, w) of interest, i.e. the ones that make a large contribution to the integral. The value of I_n increases as we move towards diagonal points with increasing v and w, due to the fact that both the numerator and the denominator approach zero at these points. However, these points make a small contribution to the coagulation source term.

4.2.1. *Effect of fluctuations on the zeroth moment*

The transport equation for the time-averaged zeroth moment, $\overline{M_0}$, is obtained from (4.4) for $k = 0$ as

$$\bar{u}_j \frac{\partial \overline{M_0}}{\partial x_j} + \frac{\partial \overline{u_j' M_0'}}{\partial x_j} = \frac{1}{Sc}\frac{1}{Re}\frac{\partial^2 \overline{M_0}}{\partial x_j \partial x_j} + Da_{coag}\left(-\frac{1}{2}\int_0^\infty\int_0^\infty \beta(v,w)\,\bar{n}(v)\,\bar{n}(w)\,\mathrm{d}v\,\mathrm{d}w - \frac{1}{2}\int_0^\infty\int_0^\infty \beta(v,w)\,\overline{n'(v)\,n'(w)}\,\mathrm{d}v\,\mathrm{d}w\right). \tag{4.6}$$

In this section, we focus on the correlations arising from the Reynolds decomposition of the coagulation source term. This decomposition is shown below, with the terms labelled as A_0, B_0 and C_0 to facilitate the subsequent discussion:

$$\underbrace{-\frac{1}{2}\int_0^\infty\int_0^\infty \beta(v,w)\,\overline{n(v)\,n(w)}\,\mathrm{d}v\,\mathrm{d}w}_{A_0} = \underbrace{-\frac{1}{2}\int_0^\infty\int_0^\infty \beta(v,w)\,\bar{n}(v)\,\bar{n}(w)\,\mathrm{d}v\,\mathrm{d}w}_{B_0} \underbrace{-\frac{1}{2}\int_0^\infty\int_0^\infty \beta(v,w)\,\overline{n'(v)\,n'(w)}\,\mathrm{d}v\,\mathrm{d}w}_{C_0}. \tag{4.7}$$

A contour plot of the absolute values of A_0 and a contour plot of C_0 for $Da_{coag} = 1/3$ are depicted in figures 12(*a*) and 12(*b*), respectively (because of to symmetry, only the top half is shown). The term C_0 is unclosed and is usually neglected in studies of turbulent coagulation; C_0 attains the maximum value close to the orifice and in particular at the shear layer between the jet stream with the co-flow stream. In this

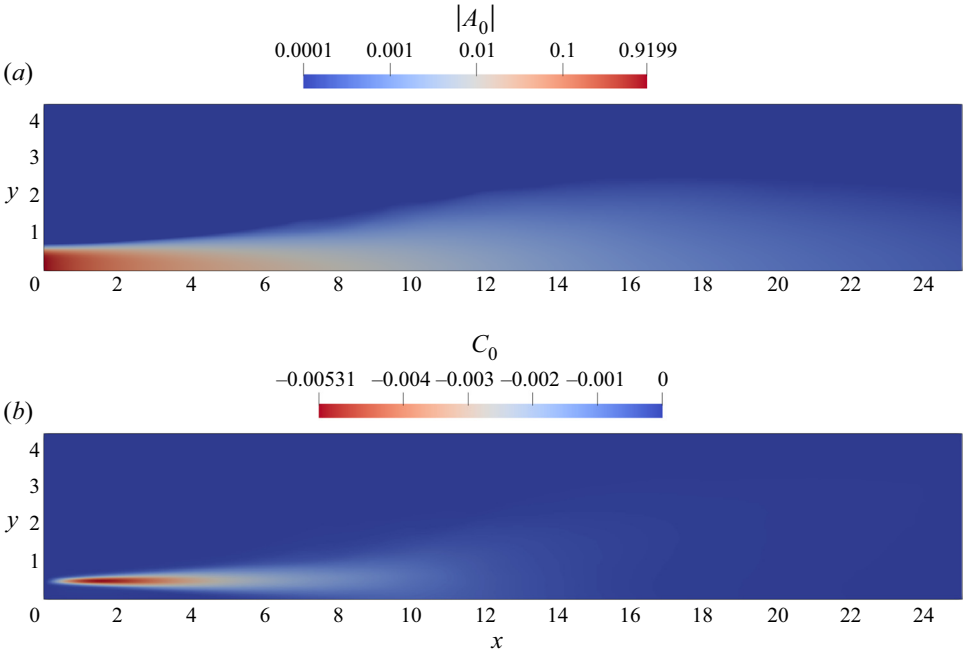

Figure 12. Contour plots of $|A_0|$ (*a*) and C_0 (*b*) for $Da_{coag} = 1/3$. A logarithmic scale colourbar was used in (*a*).

region, Kelvin–Helmholtz instabilities develop, leading to vortical structures, and also the magnitude of the coagulation source term of the M_0 equation is very large close to the inlet. An important observation is that C_0 is negative everywhere in the domain, because for most v, w combinations, the correlations $\overline{n'(v)\,n'(w)}$ were found to be positive, as was discussed before and shown in figure 9. The fact that $C_0 < 0$ means that, by neglecting it, one would overestimate $\overline{M_0}$. Qualitatively, this is also in agreement with the results of Garrick (2011), where it was found that the predominant effect of the SGS contribution is to reduce particle growth.

The evolution of A_0 for both Da_{coag} numbers is depicted in figure 13. Solid lines were used for the case of $Da_{coag} = 1$, and dashed lines for $Da_{coag} = 1/3$. The values of A_0 along the centreline are shown in figure 13(*a*), where a logarithmic scale was used for the y axis. It is observed that A_0 is larger in magnitude for the low Da_{coag} case, and its values cover a range of four orders of magnitude. Close to the inlet, similarly to $\overline{M_0}$, A_0 attains the highest magnitude, which is $O(1)$. This is a region of rapid coagulation due to the high particle concentration. The value of A_0 drops rapidly with the distance from the orifice and eventually takes values that are $O(10^{-5})$ close to the outlet.

The cross-stream profiles at the axial position $x = 20$ – where self-similarity is verified by both simulations – of each term in (4.7) are shown in figure 13(*b*). It is observed that the maximum magnitude of C_0 is not found on the centreline. Specifically, C_0 increases as we move from the centreline to the jet edges, reaches its maximum value, and then decreases. This picture is consistent with the contour plot shown in figure 12. This behaviour is similar to that found for the TKE and the passive scalar fluctuations $\sqrt{\overline{\phi'^2}}$ profiles. The horizontal axes in figures 13(*b*) and 14(*b*) are non-dimensionalised with $\delta_\phi = 2.362$ (the jet half-width based on the passive scalar for the axial position $x = 20$).

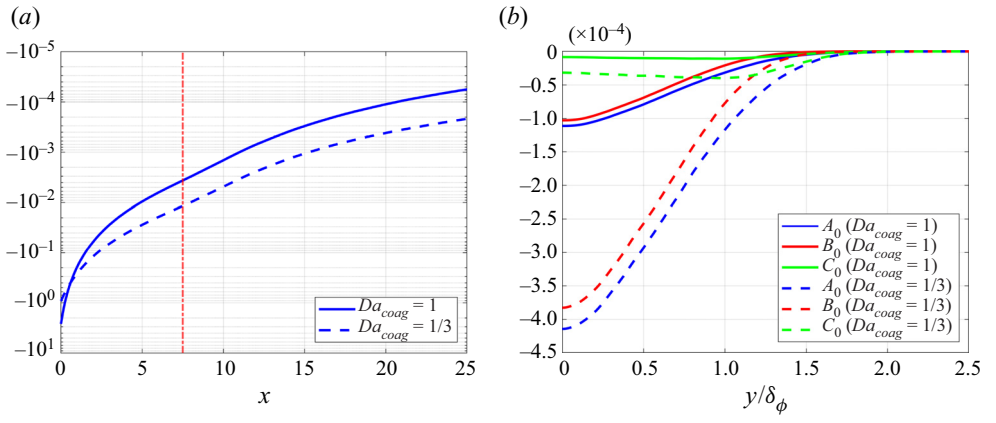

Figure 13. Coagulation source terms for the zeroth moment (see (4.7)). (*a*) Centreline values of A_0; the red dashed-dotted line indicates the jet break-up location. (*b*) Cross-stream profiles of A_0, B_0 and C_0 at the axial position $x = 20$. A logarithmic scale was used for the vertical axis in (*a*). The horizontal axis in (*b*) was normalised by $\delta_\phi = 2.362$. Note the different horizontal axes in (*a*) and (*b*).

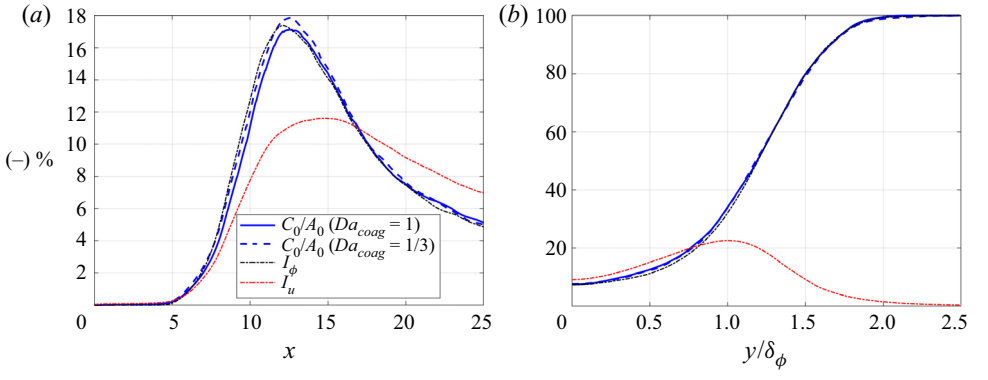

Figure 14. C_0/A_0 ratio (see (4.7)). (*a*) Centreline values of C_0/A_0. (*b*) Cross-stream profiles of C_0/A_0 at the axial position $x = 20$. The horizontal axis in (*b*) was normalised by $\delta_\phi = 2.362$. Note the different horizontal axes in (*a*) and (*b*).

To elucidate further the effect of turbulent fluctuations on coagulation, the relative contribution of each term on the right-hand side of (4.7) is examined. Here, C_0 is normalised by A_0, and the results along the centreline for both Da_{coag} values are shown in figure 14(*a*). The ratio C_0/A_0 represents the contribution of the number density fluctuations to the total coagulation source term. It can also be seen that C_0/A_0 seems to have a weak dependence on Da_{coag} (figures 14*a*,*b*). The centreline values of C_0/A_0 are zero close to the inlet. The ratio starts to increase after the jet break-up, and reaches the value 18 % at $x = 12.4$. After this point, the ratio gradually decreases and reaches the value 5 % at the exit of the computational domain. It can be seen that at the centreline, C_0 makes a significant contribution (approximately 20 %) to the mean source term A_0.

This contribution increases close to the jet edges, as shown by the cross-stream profiles of C_0/A_0 plotted in figure 14(*b*) for $x = 20$ for both Da_{coag} cases. For example, at $y/\delta_\phi = 1$, the ratio C_0/A_0 has values between 30 % and 40 %. In other words, as the jet spreads, the difference between B_0 and A_0 increases, and at the point where the value

of the first moment ($M_1 \equiv \phi$) has dropped to half of the value on the centreline, the difference has reached a value between 30 % and 40 %. Further away from the centreline, both A_0 and C_0 assume very small values and therefore no significance can be ascribed to their ratio, which approaches 1 as $C_0/A_0 = 1 - B_0/A_0$ and B_0 approaches zero. The same behaviour was also found for I_ϕ. Nevertheless, the region far away from the centreline is not of interest, since the number concentration of particles is also very small. From this discussion, it can be concluded that C_0 should not be neglected in the modelling of turbulent coagulation.

For comparison purposes, the squares of the passive scalar fluctuations intensity, I_ϕ, and the velocity fluctuations intensity, I_u, are also shown in figure 14. An interesting observation is that C_0/A_0 has qualitatively and quantitatively the same behaviour as I_ϕ. Dilution due to turbulent mixing (rather than coagulation) was found to have a slightly greater effect on the evolution of M_0, as was discussed in § 4.1. This partly explains why C_0/A_0 behaves like I_ϕ.

4.2.2. *Effect of fluctuations on the second moment*

The analysis of the previous section is now performed for the second moment. The transport equation of $\overline{M_2}$ can be derived by setting $k = 2$ into (4.4), which results in

$$\bar{u}_j \frac{\partial \overline{M_2}}{\partial x_j} + \frac{\partial \overline{u_j' M_2'}}{\partial x_j} = \frac{1}{Sc}\frac{1}{Re}\frac{\partial^2 \overline{M_2}}{\partial x_j \partial x_j} + Da_{coag}\left(\int_0^\infty \int_0^\infty vw\,\beta(v,w)\,\bar{n}(v)\,\bar{n}(w)\,\mathrm{d}v\,\mathrm{d}w + \int_0^\infty \int_0^\infty vw\,\beta(v,w)\,\overline{n'(v)\,n'(w)}\,\mathrm{d}v\,\mathrm{d}w\right). \tag{4.8}$$

The correlations arising from the Reynolds decomposition of the coagulation source term are labelled as follows:

$$\underbrace{\int_0^\infty \int_0^\infty vw\,\beta(v,w)\,\overline{n(v)\,n(w)}\,\mathrm{d}v\,\mathrm{d}w}_{A_2} = \underbrace{\int_0^\infty \int_0^\infty vw\,\beta(v,w)\,\bar{n}(v)\,\bar{n}(w)\,\mathrm{d}v\,\mathrm{d}w}_{B_2} + \underbrace{\int_0^\infty \int_0^\infty vw\,\beta(v,w)\,\overline{n'(v)\,n'(w)}\,\mathrm{d}v\,\mathrm{d}w}_{C_2}. \tag{4.9}$$

The evolution of A_2 and C_2 for $Da_{coag} = 1/3$ is shown in figure 15. The value of the term C_2 is positive everywhere in the domain, again because $\overline{n'(v)\,n'(w)}$ is mostly positive, as discussed before. This implies that neglecting C_2 would lead to an underestimation of $\overline{M_2}$. Figure 15(*b*) shows that away from the centreline towards the jet edges, C_2 increases until reaching a local maximum, at roughly $(x, y) = (9, 0.55)$ for both runs, and then drops to zero. The maximum is located slightly downstream of the jet break-up and coincides with the location where the r.m.s. value of the passive scalar fluctuations $\sqrt{\overline{\phi'^2}}$ is maximised. For reference, the location of the maximum TKE is $(x, y) = (11, 0.7)$.

The variation of A_2 in the centreline is shown in figure 16(*a*) for both Da_{coag} numbers. In the absence of flow, A_2 would increase monotonically with time. Indeed, this is exactly what happens close to the jet nozzle; A_2 increases with distance away from the orifice (time can be converted easily to distance). Shortly upstream of the jet break-up location (red dashed-dotted line in figure 16*a*), A_2 starts to decrease and eventually reaches values

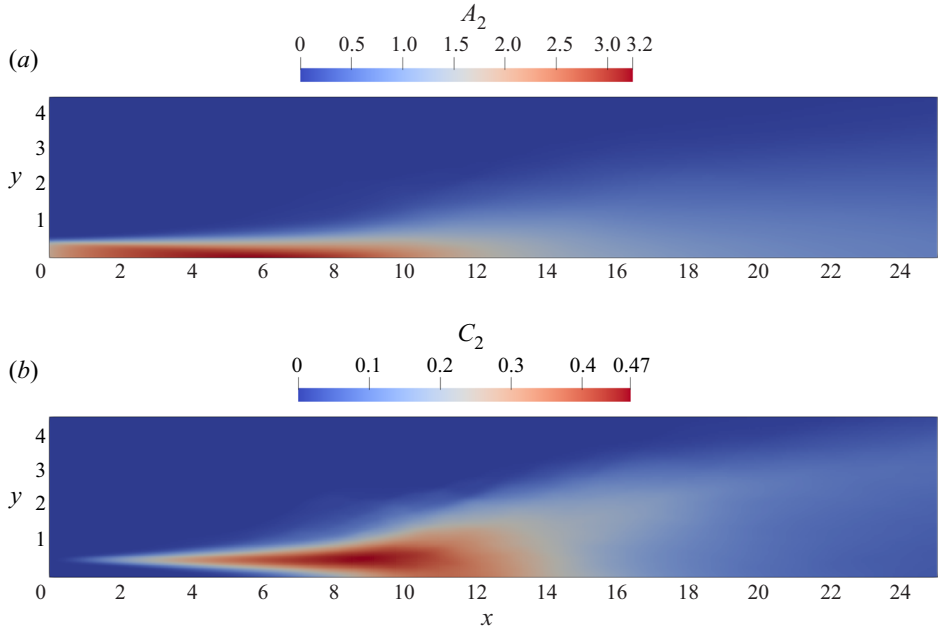

Figure 15. Contour plots of A_2 (*a*) and C_2 (*b*) for $Da_{coag} = 1/3$.

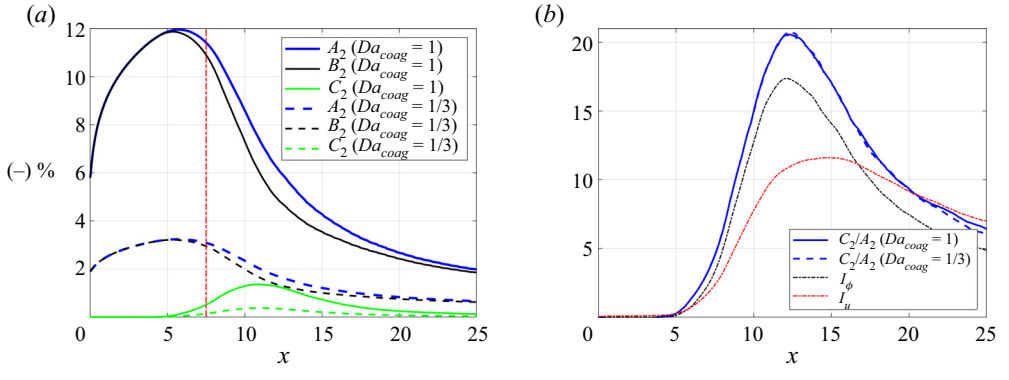

Figure 16. Coagulation source terms of the second moment equation (see (4.9)). (*a*) Centreline values of A_2, B_2 and C_2; the red dashed-dotted line indicates the jet break-up location. (*b*) Centreline values of ratio C_2/A_2.

smaller even than those at the inlet. The maximum of C_2 along the centreline is found at around $x = 11$. The highest deviation between A_2 and B_2 is found in the region between $x = 7.5$ and 18, and this is true for both Da_{coag} numbers. It is also noted that even though A_2 is reduced, the effect of coagulation can compensate for the effect of turbulent dilution on mean M_2; this can be concluded from the fact that the latter increases in the streamwise direction, as shown in figure 8(*b*).

The variation of the ratio C_2/A_2 along the centreline is depicted in figure 16(*b*). This ratio represents the relative contribution of the number density fluctuations to the total source term. Note that C_2/A_2 was found to have a weak dependence on Da_{coag} for the cases examined, similar to C_0/A_0. The maximum along the centreline is 20.6 % and is found at $x = 12.5$, while the peak value of C_0/A_0 was around 17.5 % found at the same

location x. It can be seen that C_2 makes a large contribution to A_2 and therefore should not be neglected for accurate modelling of turbulent coagulation.

For comparison purposes, the squares of the passive scalar fluctuations intensity $I_\phi = \overline{\phi'^2}/\overline{\phi^2}$ and the velocity fluctuations intensity $I_u = \overline{u_i'^2}/\overline{U_i^2}$ are also shown in figure 16(b). An interesting observation is that C_2/A_2 reaches higher values than the ratio C_0/A_0. It was shown in § 4.2.1 that C_0/A_0 reaches values close to I_ϕ (see figure 14a). On the contrary, it is observed from figure 16(b) that the relative difference between the peak value of C_2/A_2 and that of I_ϕ is 18 %. Coagulation was found to have a greater effect on the evolution of M_2 in this region, as discussed in § 4.1. This has to do with the heavier weighting of the large particles of the distribution, which are formed due to coagulation at downstream positions, on the second moment. On the other hand, turbulent dilution (rather than coagulation) was found to have a slightly stronger effect on the evolution of M_0. This partly explains why C_2/A_2 reaches higher values than the ratio C_0/A_0.

5. Conclusions

The objective of the present paper was to present a DNS study of turbulence–coagulation interaction. In particular, the study focused on the behaviour and significance of the unknown correlations of fluctuations that arise from the Reynolds decomposition of the PBE and moment transport equations. These correlations appear in any problem featuring turbulence and coagulation, such as soot formation and nanoparticle synthesis, but usually in conjunction with other physical and chemical effects, such as those associated with chemical kinetics. Hence the numerical experiments in the present study are intended to isolate the effect of turbulence–coagulation interaction. The numerical experiments were conducted in the Eulerian DNS–PBE framework, where the DNS resolves the flow down to the Kolmogorov scale, while the PBE is solved via a discretisation method that is free of *a priori* assumptions regarding the shape of the PSD. A unity Schmidt number was employed, as it is not feasible at present to resolve the Batchelor scales that result from diffusion at high Schmidt numbers. Direct numerical simulations of a 3-D turbulent planar jet flow at $Re = 3000$ were performed, for which it was feasible to obtain a fully resolved turbulent flow as well as an accurate numerical solution of the PBE in the whole domain, and the flow field was validated by comparison with reference experimental and DNS data. The jet was laden with monodispersed nanoparticles issued into a particle-free co-flow stream. The phenomena under investigation were turbulent mixing and particle coagulation in the free-molecule regime. Simulations for two different coagulation Damköhler numbers, $Da_{coag} = 1$ and $1/3$, were carried out, where Da_{coag} is defined as the ratio of a convection time scale to a coagulation time scale, the latter related to the time needed to reach the self-preserving distribution.

The correlations of the fluctuating number densities were calculated at specific probe points in the domain. It was found that the correlations were mostly positive for all combinations of particle volumes. However, negative correlations were also present for the case of more intense coagulation, i.e. $Da_{coag} = 1$, close to the jet break-up location. Furthermore, the intensity of the correlations was examined by normalising them with the mean of the product of the number densities. Results showed that the intensity maps have rather uniform values with magnitude close to the square of the passive scalar fluctuations intensity.

Unclosed terms also arise during the Reynolds decomposition of the transport equations for the zeroth and second moments. The unclosed terms make a large contribution to the time-averaged coagulation source terms and therefore should not be neglected. More

specifically, for the transport equation of $\overline{M_0}$, the ratio of the term with the unknown correlations (denoted C_0) to the time-averaged coagulation source term (denoted A_0) reaches values as high as 18 % on the jet centreline, and increases up to 40 % close to the jet edges. Furthermore, the value of C_0 was negative everywhere in the domain because, for most particle size combinations, the correlations of the fluctuating number densities were found to be positive. The negative value of C_0 indicates that neglect of C_0 could lead to an overestimation of $\overline{M_0}$. For the transport equation of $\overline{M_2}$, the ratio of the term with the unknown correlations (denoted C_2) to the time-averaged coagulation source term (denoted A_2) reached values as high as 20 % on the jet centreline, and the value of C_2 was positive everywhere in the domain.

In the present flow configuration, the ratio C_0/A_0 showed the same behaviour as that of the square of the passive scalar fluctuations intensity. This indicates that dilution due to turbulent mixing (rather than coagulation) had a slightly greater effect on the evolution of M_0 in the region downstream of the jet break-up location. On the contrary, C_2/A_2 was found to reach higher values than C_0/A_0, with a relative difference of the peak values close to 18 %, indicating that coagulation (rather than turbulent dilution) had a greater effect on the evolution of M_2. Finally, both ratios were found to have a weak dependence on the Da_{coag} number, at least for the cases examined.

To summarise, the present study aimed to refine our understanding of the effect of turbulent fluctuations on the coagulation process. Coagulation is a key process in several engineering and environmental problems – including soot formation, flame synthesis of nanoparticles such as silica and titania, and atmospheric aerosols – and understanding its interaction with turbulence is important for developing judicious assumptions and developing accurate models for predicting particle-laden flows. Future work should examine these interactions within more complex flows and in situations where other particulate phenomena, such as nucleation and growth, are present.

Funding. The authors are grateful to the Leverhulme Trust for financial support (grant reference RPG-2018-101). The authors also wish to acknowledge the UK Consortium on Turbulent Reacting Flows (www.ukctrf.com) for providing access to the ARCHER facility through EPSRC grant EP/R029369/1, as well as the UK Materials and Molecular Modelling Hub for computational resources on THOMAS through EPSRC grant EP/P020194/1.

Declaration of interests. The authors report no conflict of interest.

Author ORCIDs.
Malamas Tsagkaridis https://orcid.org/0000-0001-9649-9341;
Stelios Rigopoulos https://orcid.org/0000-0002-0311-2070;
George Papadakis https://orcid.org/0000-0003-0594-3107.

Appendix A

The turbulent kinetic energy (TKE) equation takes the form (Pope 2000)

$$\underbrace{-\bar{u}_j \frac{\partial}{\partial x_j}\left(\frac{1}{2}\overline{u_i' u_i'}\right)}_{C_k} \underbrace{-\frac{\partial}{\partial x_j}\left(\frac{1}{\rho}\overline{u_j' p'}\right)}_{\pi_k} \underbrace{-\frac{\partial}{\partial x_j}\left(\frac{1}{2}\overline{u_i' u_i' u_j'}\right)}_{T_k}$$
$$\underbrace{+\frac{\partial}{\partial x_j}\left(2\nu\,\overline{u_i' s_{ij}}\right)}_{D_k} \underbrace{-\overline{u_i' u_j'} S_{ij}}_{P_k} \underbrace{-2\nu\,\overline{s_{ij} s_{ij}}}_{\epsilon_k} = 0, \tag{A1}$$

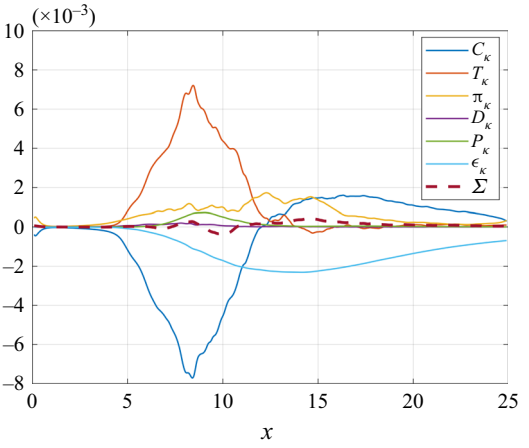

Figure 17. Variation of turbulent kinetic energy budgets along the jet centreline (all terms are non-dimensionalised with the variables defined in (2.3*a–d*)).

where S_{ij} and s_{ij} denote the mean and fluctuating strain rates, respectively:

$$S_{ij} = \frac{1}{2}\left(\frac{\partial \bar{u}_i}{\partial x_j} + \frac{\partial \bar{u}_j}{\partial x_i}\right), \quad s_{ij} = \frac{1}{2}\left(\frac{\partial u'_i}{\partial x_j} + \frac{\partial u'_j}{\partial x_i}\right). \tag{A2a,b}$$

In (A1), terms C_k, π_k, T_k, D_k, P_k and ϵ_k denote convection due to mean flow, pressure gradient work, transport by velocity fluctuations, viscous diffusion, production by mean flow, and dissipation, respectively. The variation of these terms together with their sum, Σ, along the jet centreline is shown in figure 17. Overall, the equation is well balanced, with the maximum error being less than 5.5 % of the peak absolute value of convection due to mean flow. This indicates that the resolution of the computational grid is fine enough.

Figure 18 shows the one-dimensional $E_{11}(\kappa_1)$ and $E_{22}(\kappa_1)$ spectra of turbulent fluctuations, plotted with Kolmogorov scaling. For the definition of these quantities, we refer to Pope (2000). The spectra are presented as functions of streamwise wavenumber κ_1, and they were obtained from the frequency spectra of the streamwise and cross-stream velocity fluctuations at the probe point $(x, y, z) = (20, 1.5, 0)$, which is located in the region of fully developed turbulence. The conversion of the frequency to wavenumber spectra is based on Taylor's 'frozen turbulence' hypothesis (Taylor 1935) and was performed through the variable transformation $\kappa_1 = 2\pi f/U_c$, where f is the frequency, and U_c is a convection velocity taken as the time-averaged streamwise velocity at that probe point. The Kolmogorov $-5/3$ power-law one-dimensional spectra $E_{11}(\kappa_1) = C_1\,\epsilon^{2/3}\,\kappa_1^{-5/3}$ and $E_{22}(\kappa_1) = C'_1\,\epsilon^{2/3}\,\kappa_1^{-5/3}$ were also calculated using the value of the turbulent kinetic energy dissipation rate at that probe point and presented in the figures for comparison. The values of the universal constants C_1 and C'_1 are 0.49 and 0.65, respectively (Pope 2000). Although, for the flow conditions examined, an extended inertial region is not expected, the DNS data do exhibit a power-low close to $-5/3$ over about a decade, and match well the theoretical spectra. Furthermore, at high frequencies, a dissipative range with a faster decay rate is observed, which indicates that the turbulent motions are well resolved.

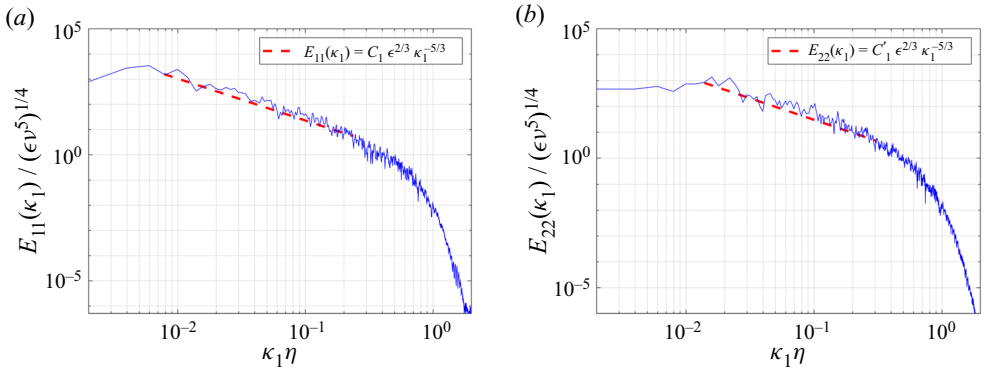

Figure 18. One-dimensional power spectra $E_{11}(\kappa_1)$ (*a*) and $E_{22}(\kappa_1)$ (*b*) obtained from the frequency spectra of the streamwise and cross-stream velocity fluctuations at the probe point $(x, y, z) = (20, 1.5, 0)$. Kolmogorov's universal scaling was used. The dashed red lines represent the one-dimensional wavenumber spectra (*a*) $E_{11}(\kappa_1) = C_1 \epsilon^{2/3} \kappa_1^{-5/3}$ and (*b*) $E_{22}(\kappa_1) = C'_1 \epsilon^{2/3} \kappa_1^{-5/3}$. Logarithmic scales were used for both axes.

References

Alves Portela, F., Papadakis, G. & Vassilicos, J.C. 2020 The role of coherent structures and inhomogeneity in near-field interscale turbulent energy transfers. *J. Fluid Mech.* **896**, A16.

Balay, S., *et al.* 2021 PETSc users manual. *Tech. Rep*. ANL-95/11 – Revision 3.15. Argonne National Laboratory.

Brock, J.R., Kuhn, P.J. & Zehavi, D. 1986 Condensation aerosol formation and growth in a laminar coaxial jet: experimental. *J. Aerosol Sci.* **17** (1), 11–22.

Browne, L.W.B., Antonia, R.A., Rajagopalan, S. & Chambers, A.J. 1983 Interaction region of a two-dimensional turbulent plane jet in still air. In *Structure of Complex Turbulent Shear Flow*, pp. 411–419. Springer.

Buesser, B. & Pratsinis, S.E. 2012 Design of nanomaterial synthesis by aerosol processes. *Annu. Rev. Chem. Biomol. Engng* **3**, 103–127.

Cifuentes, L., Sellmann, J., Wlokas, I. & Kempf, A. 2020 Direct numerical simulations of nanoparticle formation in premixed and non-premixed flame-vortex interactions. *Phys. Fluids* **32** (9), 093605.

Das, S. & Garrick, S.C. 2010 The effects of turbulence on nanoparticle growth in turbulent reacting jets. *Phys. Fluids* **22** (10), 103303.

Davidson, P.A. 2004 *Turbulence An Introduction for Scientists and Engineers*. Oxford University Press.

Davies, A.E., Keffer, J.F. & Baines, W.D. 1975 Spread of a heated plane turbulent jet. *Phys. Fluids* **18** (7), 770–775.

Delichatsios, M.A. & Probstein, R.F. 1975 Coagulation in turbulent flow: theory and experiment. *J. Colloid Interface Sci.* **51** (3), 394–405.

Deo, R.C., Mi, J. & Nathan, G.J. 2008 The influence of Reynolds number on a plane jet. *Phys. Fluids* **20** (7), 075108.

Di Veroli, G. & Rigopoulos, S. 2009 A study of turbulence-chemistry interaction in reactive precipitation via a population balance-transported PDF method. In *Turbulence, Heat and Mass Transfer 6. Proceedings of the Sixth International Symposium on Turbulence, Heat and Mass Transfer, Rome, Italy* (ed. K. Hanjalić, Y. Nagano & S. Jakirlić). Begell House.

Di Veroli, G. & Rigopoulos, S. 2010 Modeling of turbulent precipitation: a transported population balance-PDF method. *AIChE J.* **56** (4), 878–892.

Di Veroli, G.Y. & Rigopoulos, S. 2011 Modeling of aerosol formation in a turbulent jet with the transported population balance equation-probability density function approach. *Phys. Fluids* **23** (4), 043305.

Drake, R.L. 1972 A general mathematical survey of the coagulation equation. In *Topics in Current Aerosol Research, Part 2* (ed. G.M. Hidy), International Reviews in Aerosol Physics and Chemistry, vol. 3, pp. 204–376. Pergamon Press.

Drossinos, Y. & Housiadas, C. 2006 Aerosol flows. In *Multiphase Flow Handbook* (ed. C.T. Crowe), pp. 6-1–6-58. CRC Press.

ELGHOBASHI, S. 2006 An updated classification map of particle-laden turbulent flows. *Fluid Mech. Appl.* **81**, 3–10.

FRIEDLANDER, S.K. 2000 *Smoke, Dust, and Haze: Fundamentals of Aerosol Dynamics*, 2nd edn. Oxford University Press.

GARRICK, S.C. 2011 Effects of turbulent fluctuations on nanoparticle coagulation in shear flows. *Aerosol Sci. Technol.* **45** (10), 1272–1285.

GARRICK, S.C. & KHAKPOUR, M. 2004 The effects of differential diffusion on nanoparticle coagulation in temporal mixing layers. *Aerosol Sci. Technol.* **38** (8), 851–860.

GARRICK, S.C., LEHTINEN, K.E.J. & ZACHARIAH, M.R. 2006 Nanoparticle coagulation via a Navier–Stokes/Nodal methodology: evolution of the particle field. *J. Aerosol Sci.* **37** (5), 555–576.

GOUDELI, E. & PRATSINIS, S.E. 2016 Gas-phase manufacturing of nanoparticles: molecular dynamics and mesoscale simulations. *Part. Sci. Technol.* **34** (4), 483–493.

GUTMARK, E. & WYGNANSKI, I. 1976 The planar turbulent jet. *J. Fluid Mech.* **73** (3), 465–495.

JASAK, H., WELLER, H.G. & GOSMAN, A.D. 1999 High resolution NVD differencing scheme for arbitrarily unstructured meshes. *Intl J. Numer. Meth. Fluids* **31** (2), 431–449.

JENKINS, P.E. & GOLDSCHMIDT, V.W. 1973 Mean temperature and velocity in a plane turbulent jet. *Trans. ASME J. Fluids Engng* **95** (4), 581–584.

JUNZONG, Z., HAIYING, Q. & JINSHENG, W. 2013 Nanoparticle dispersion and coagulation in a turbulent round jet. *Intl J. Multiphase Flow* **54**, 22–30.

KLEIN, M., SADIKI, A. & JANICKA, J. 2003*a* A digital filter based generation of inflow data for spatially developing direct numerical or large eddy simulations. *J. Comput. Phys.* **186** (2), 652–665.

KLEIN, M., SADIKI, A. & JANICKA, J. 2003*b* Investigation of the influence of the Reynolds number on a plane jet using direct numerical simulation. *Intl J. Heat Fluid Flow* **24** (6), 785–794.

KULMALA, M., VEHKAMÄKI, H., PETÄJÄ, T., DAL MASO, M., LAURI, A., KERMINEN, V.-M., BIRMILI, W. & MCMURRY, P.H. 2004 Formation and growth rates of ultrafine atmospheric particles: a review of observations. *J. Aerosol Sci.* **35** (2), 143–176.

LANDGREBE, J.D. & PRATSINIS, S.E. 1990 A discrete-sectional model for particulate production by gas-phase chemical reaction and aerosol coagulation in the free-molecular regime. *J. Colloid Interface Sci.* **139** (1), 63–86.

LE RIBAULT, C., SARKAR, S. & STANLEY, S.A. 1999 Large eddy simulation of a plane jet. *Phys. Fluids* **11** (10), 3069–3083.

LEVICH, V.G. 1962 *Physicochemical Hydrodynamics*. Prentice-Hall.

LEVIN, L.M. & SEDUNOV, Y.S. 1966 Gravitational coagulation of charged cloud drops in turbulent flow. *Pure Appl. Geophys.* **64** (1), 185–196.

LEVIN, L.M. & SEDUNOV, Y.S. 1968 The theoretical model of the drop spectrum formation process in clouds. *Pure Appl. Geophys.* **69** (1), 320–335.

LIU, A. & RIGOPOULOS, S. 2019 A conservative method for numerical solution of the population balance equation, and application to soot formation. *Combust. Flame* **205**, 506–521.

MILLER, S.E. & GARRICK, S.C. 2004 Nanoparticle coagulation in a planar jet. *Aerosol Sci. Technol.* **38** (1), 79–89.

OLIN, M., RÖNKKÖ, T. & DAL MASO, M. 2015 CFD modeling of a vehicle exhaust laboratory sampling system: sulfur-driven nucleation and growth in diluting diesel exhaust. *Atmos. Chem. Phys.* **15** (9), 5305–5323.

PESMAZOGLOU, I., KEMPF, A.M. & NAVARRO-MARTINEZ, S. 2017 Large eddy simulation of particle aggregation in turbulent jets. *J. Aerosol Sci.* **111**, 1–17.

POPE, S.B. 2000 *Turbulent Flows*. Cambridge University Press.

RAJARATNAM, N. 1976 *Turbulent Jets*. Elsevier.

RAMAN, V. & FOX, R.O. 2016 Modeling of fine-particle formation in turbulent flames. *Annu. Rev. Fluid Mech.* **48**, 159–190.

RAMAPRIAN, B.R. & CHANDRASEKHARA, M.S. 1985 LDA measurements in plane turbulent jets. *Trans. ASME J. Fluids Engng* **107** (2), 264–271.

READE, W.C. & COLLINS, L.R. 2000 A numerical study of the particle size distribution of an aerosol undergoing turbulent coagulation. *J. Fluid Mech.* **415**, 45–64.

RIGOPOULOS, S. 2007 PDF method for population balance in turbulent reactive flow. *Chem. Engng Sci.* **62** (23), 6865–6878.

RIGOPOULOS, S. 2010 Population balance modelling of polydispersed particles in reactive flows. *Prog. Energy Combust. Sci.* **36** (4), 412–443.

RIGOPOULOS, S. 2019 Modelling of soot aerosol dynamics in turbulent flow. *Flow Turbul. Combust.* **103** (3), 565–604.

SAFFMAN, P.G. & TURNER, J.S. 1956 On the collision of drops in turbulent clouds. *J. Fluid Mech.* **1** (1), 16–30.

SCOTT, W.T. 1967 Poisson statistics in distributions of coalescing droplets. *J. Atmos. Sci.* **24** (2), 221–225.

SETTUMBA, N. & GARRICK, S.C. 2003 Direct numerical simulation of nanoparticle coagulation in a temporal mixing layer via a moment method. *J. Aerosol Sci.* **34** (2), 149–167.

SEWERIN, F. & RIGOPOULOS, S. 2017 An LES-PBE-PDF approach for modeling particle formation in turbulent reacting flows. *Phys. Fluids* **29** (10), 105105.

SEWERIN, F. & RIGOPOULOS, S. 2018 An LES-PBE-PDF approach for predicting the soot particle size distribution in turbulent flames. *Combust. Flame* **189**, 62–76.

SEWERIN, F. & RIGOPOULOS, S. 2019 Algorithmic aspects of the LES-PBE-PDF method for modeling soot particle size distributions in turbulent flames. *Combust. Sci. Technol.* **191** (5–6), 766–796.

DA SILVA, C.B., LOPES, D.C. & RAMAN, V. 2015 The effect of subgrid-scale models on the entrainment of a passive scalar in a turbulent planar jet. *J. Turbul.* **16** (4), 342–366.

STANLEY, S.A. & SARKAR, S. 2000 Influence of nozzle conditions and discrete forcing on turbulent planar jets. *AIAA J.* **38** (9), 1615–1623.

STANLEY, S.A., SARKAR, S. & MELLADO GONZÁLEZ, J.P. 2002 A study of the flow-field evolution and mixing in a planar turbulent jet using direct numerical simulation. *J. Fluid Mech.* **450**, 377–407.

SURESH, P.R., SRINIVASAN, K., SUNDARARAJAN, T. & DAS, S.K. 2008 Reynolds number dependence of plane jet development in the transitional regime. *Phys. Fluids* **20** (4), 044105.

TANG, H.Y., RIGOPOULOS, S. & PAPADAKIS, G. 2020 A methodology for coupling DNS and discretised population balance for modelling turbulent precipitation. *Intl J. Heat Fluid Flow* **86**, 108689.

TAYLOR, G.I. 1935 Statistical theory of turbulence. *Proc. R. Soc. Lond.* A **23** (2), 421–444.

THOMAS, F.O. & CHU, H.C. 1989 An experimental investigation of the transition of a planar jet: subharmonic suppression and upstream feedback. *Phys. Fluids* A **1** (9), 1566–1587.

VEMURY, S., KUSTERS, K.A. & PRATSINIS, S.E. 1994 Time-lag for attainment of the self-preserving particle size distribution by coagulation. *J. Colloid Interface Sci.* **165** (1), 53–59.

VEMURY, S. & PRATSINIS, S.E. 1995 Self-preserving size distributions of agglomerates. *J. Aerosol Sci.* **26** (2), 175–185.

WANG, L.P., WEXLER, A.S. & ZHOU, Y. 1998 On the collision rate of small particles in isotropic turbulence. I. Zero-inertia case. *Phys. Fluids* **10** (1), 266–276.

WARSHAW, M. 1967 Cloud droplet coalescence: statistical foundations and a one-dimensional sedimentation model. *J. Atmos. Sci.* **24** (3), 278–286.

WATANABE, T., SAKAI, Y., NAGATA, K., ITO, Y. & HAYASE, T. 2014 Vortex stretching and compression near the turbulent/non-turbulent interface in a planar jet. *J. Fluid Mech.* **758**, 754–785.

WHITBY, E.R. & MCMURRY, P.H. 1997 Modal aerosol dynamics modeling. *Aerosol Sci. Technol.* **27** (6), 673–688.

WILLIAMS, M.M.R. & LOYALKA, S.K. 1991 *Aerosol Science – Theory and Practice: With Special Applications to the Nuclear Industry*. Pergamon Press.

XIAO, D. & PAPADAKIS, G. 2019 Nonlinear optimal control of transition due to a pair of vortical perturbations using a receding horizon approach. *J. Fluid Mech.* **861**, 524–555.